




Review

Engineered Nanostructured Photocatalysts for Cancer Therapy

Javier Bonet-Aleta ^{1,2,3} , Jose I. Garcia-Peiro ^{1,2,3}  and Jose L. Hueso ^{1,2,3,*} 

¹ Institute of Nanoscience and Materials of Aragon (INMA), Campus Río Ebro, Edificio I+D, CSIC-Universidad de Zaragoza, C/Poeta Mariano Esquillor, s/n, 50018 Zaragoza, Spain; jbaleta@unizar.es (J.B.-A.); joseignacio.garcia.peiro@gmail.com (J.I.G.-P.)

² Networking Research Center in Biomaterials, Bioengineering and Nanomedicine (CIBER-BBN), Instituto de Salud Carlos III, 28029 Madrid, Spain

³ Department of Chemical and Environmental Engineering, Campus Río Ebro, University of Zaragoza, C/María de Luna, 3, 50018 Zaragoza, Spain

* Correspondence: jlhueso@unizar.es

Abstract: The present review aims at highlighting recent advances in the development of photocatalysts devoted to cancer therapy applications. We pay especial attention to the engineering aspects of different nanomaterials including inorganic semiconductors, organic-based nanostructures, noble metal-based systems or synergistic hybrid heterostructures. Furthermore, we also explore and correlate structural and optical properties with their photocatalytic capability to successfully performing in cancer-related therapies. We have made an especial emphasis to introduce current alternatives to organic photosensitizers (PSs) in photodynamic therapy (PDT), where the effective generation of reactive oxidative species (ROS) is pivotal to boost the efficacy of the treatment. We also overview current efforts in other photocatalytic strategies to tackle cancer based on photothermal treatment, starvation therapy, oxidative stress unbalance via glutathione (GSH) depletion, biorthogonal catalysis or local relief of hypoxic conditions in tumor microenvironments (TME).

Keywords: photocatalysts; photodynamic therapy; reactive oxidative species; hybrids; nanocatalysts; noble-metal; upconversion; carbon



Citation: Bonet-Aleta, J.; Garcia-Peiro, J.I.; Hueso, J.L. Engineered Nanostructured Photocatalysts for Cancer Therapy. *Catalysts* **2022**, *12*, 167. <https://doi.org/10.3390/catal12020167>

Academic Editors: Detlef W. Bahnemann, Ewa Kowalska, Ioannis Konstantinou, Magdalena Janus, Vincenzo Vaiano, Wonyong Choi and Zhi Jiang

Received: 31 December 2021

Accepted: 25 January 2022

Published: 28 January 2022

Publisher's Note: MDPI stays neutral with regard to jurisdictional claims in published maps and institutional affiliations.



Copyright: © 2022 by the authors. Licensee MDPI, Basel, Switzerland. This article is an open access article distributed under the terms and conditions of the Creative Commons Attribution (CC BY) license (<https://creativecommons.org/licenses/by/4.0/>).

1. Introduction

Cancer is still one of the major causes of death and the projections for 2050 are not optimistic, estimating around 10 MM worldwide deaths [1]. The improvement in the effectiveness of existing therapies or minimizing the side effects are considered as major goals in cancer research. Photodynamic therapy (PDT) aims at treating cancer with the aid of a photosensitizer (PS) and a light irradiation source of suitable energy to activate endogenous O₂ to produce reactive oxygen species (ROS) which subsequently provoke cell apoptosis [2]. The main advantage of this synergy is the selectivity provided by the local irradiation dosing which places PDT as a minimally invasive therapy. The light source must accomplish two main requirements: (i) the wavelength must be in the range between red (660 nm) and NIR-NIR II (1100 nm) to ensure a large tissue penetration [3] and (ii) the energy of the employed light must match with the excitation energy of the selected PSs. PSs consist of organic molecules (e.g., porfimer sodium, aminolevulinic acid, talaporfin, temoporfin or verteporfin [4]) which are being evaluated in clinical trials. These PSs are currently yielding promising results in diverse tumors [5] including esophageal [6], breast cancer [7] or melanoma [8]. However, organic-based PSs face several challenges: (i) their molecular structure is mainly based on highly conjugated π -systems formed from aromatic rings which limits their solubility in aqueous media and in biological environments [2,9]; (ii) The generated ROS, once the PS is activated with light, can react with the PS, modifying its molecular structure and hence their energetic levels. As a result, the modified PSs will not be able to interact with the light, losing its photo-activity [2]; and (iii), when PSs are

loaded on carriers, they suffer from uncontrollable loading/release, which may affect to healthy cells placed nearby the tumor region [10–12].

In the recent years, several photoactive nanocatalysts have emerged as promising candidates in phototherapy overcoming the challenges faced by organic PSs. Through a plethora of synthetic strategies, the surface of nanoparticles can be tailored with different ligands/agents to promote their stability in physiological media. Moreover, their structured nature confer them more robustness towards ROS self-production. Finally, their nanosized dimensions favor their accumulation in solid tumors due to enhanced permeability and retention (EPR) effects [13].

Organic molecules present an electronic structure organized in molecular orbitals where the energy levels own discrete values (Figure 1a) [14]. The light employed in PDT aims to interact with electrons occupying the highest occupied molecular orbital (HOMO) and promote its excitation to the lowest unoccupied molecular orbital (LUMO) [15]. This excited electron may transfer its excess of energy to a nearby O_2 molecule, change its electronic multiplicity and hence form singlet oxygen 1O_2 (process known as PDT Type I). Alternatively, it can be directly transferred to O_2 in order to boost formation of different ROS species such as superoxide anion, hydrogen peroxide or hydroxyl radicals (e.g., $\bullet O_2^-$, H_2O_2 or $\bullet OH$) (described as PDT Type II).

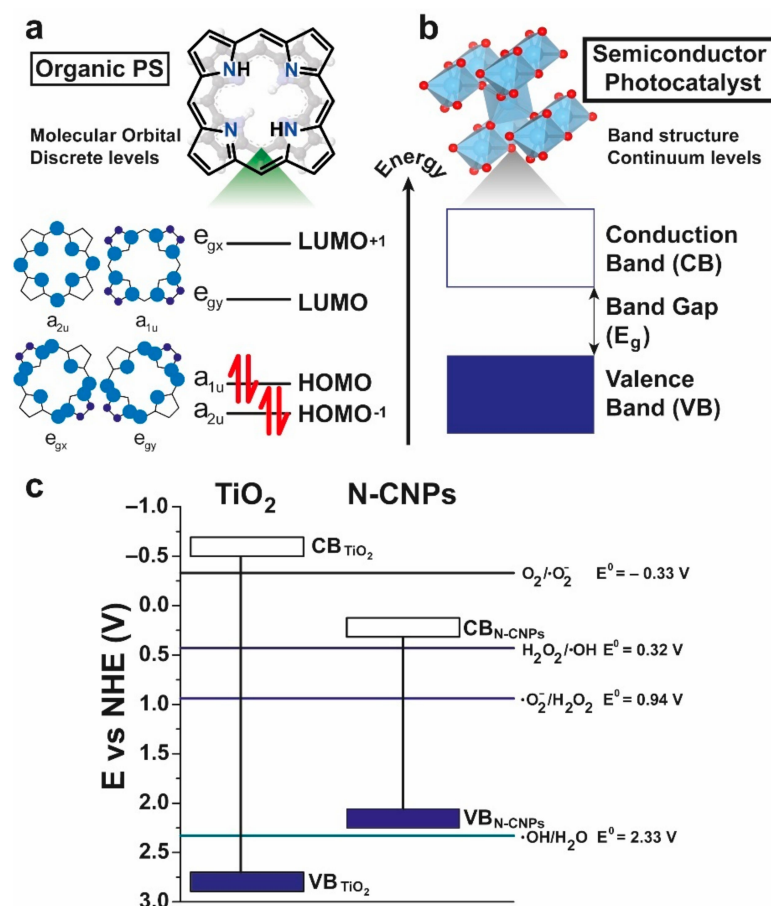


Figure 1. Differences in the electronic structure between organic PSs and semiconductor photocatalysts: (a,b) Organic molecules organize their electronic levels in molecular orbitals with discrete values in contradistinction to a classic solid semiconductor where the electronic levels acquire continuum values in bands. The most interesting bands regarding photocatalysis are the highlighted VB and CB, which are separated by E_g ; (c) Influence of the position of VB and CB in the photocatalytic products. For example, the photogenerated h^+ of a VB positioned above $E^0(\bullet OH/H_2O)$ will not possess the enough potential to oxidize H_2O into $\bullet OH$.

Unlike organic molecules, nanostructured semiconductor photocatalysts possess a band structure where the energy levels have continuum values [16]. The bands analogous to HOMO and LUMO levels in organic molecules are the valence (VB) and conduction bands (CB), respectively. They are separated by an energy corresponding to an energy band gap (E_g) in the case of semiconductors (Figure 1b). Thus, the photocatalytic event occurs when a photon with larger energy than E_g excites an electron (e^-) from VB to CB, generating electron/hole (e^-/h^+) pairs which can react with surrounding molecules such as O_2 and H_2O to generate ROS [16]. For photocatalytic therapy purposes, the energy band engineering of nanomaterials must be framed within the range of the biocompatible window (650–1100 nm). Although the E_g value is a key factor in the selection of the photocatalyst, the position of their respective bands is equally essential towards a successful ROS generation [17–19]. Considering the reduction standard potentials vs. a standard hydrogen electrode (SHE) at pH = 7 of different oxygen containing species (Figure 1c) [20], the bands of two different photocatalysts (inorganic TiO_2 and organic N-containing carbon dots) are compared with the E^0 of the half-reactions to produce ROS. Since the VB and CB of TiO_2 possess large potential levels, the reactivity of the photogenerated electron-hole pair (e^-/h^+) in TiO_2 is large, being able to oxidize H_2O into $\bullet OH$ and reduce O_2 into $\bullet O_2^-$. Despite the efficiency of TiO_2 as a photocatalyst, its wide E_g (3.2 eV) burdens its direct application for in vivo photocatalysis, as the energy of the required light is 385 nm and its penetration in tissues is close to zero [3]. On the other hand, while nitrogen-doped carbon dots (N-CDs) with a narrower E_g (1.63 eV) can be activated with 650 nm biocompatible-light, the position of their VB prevents the formation of hydroxyl radicals ($\bullet OH$) from H_2O , a desired ROS from the therapeutic point of view. Figure 1 summarizes two examples of well-known standing alone photocatalysts that are not suitable for PDT but might work if conveniently engineered to form a hybrid heterostructure.

The use of nanostructured photocatalysts does not only tackle ROS generation to perform PDT. Recent literature reports also confer on them the capability to catalyze water splitting (i.e., O_2 production from H_2O) [21], glutathione (GSH) oxidation [22] and H_2 production [23]. Since PDT employs O_2 as the major electron/energy acceptor to generate ROS, its intrinsic scarcity in the tumor environment typically burdens the full potential of this therapy. The aberrant growth of tumors provokes an irregular creation of blood vessels causing limited O_2 supply [24]. Thus, the in-situ generation of O_2 is considered a major advantage for a photocatalyst because of the continuous photogeneration of ROS in a hypoxic environment [25]. Regarding GSH, its key role as the main antioxidant molecule in animal cells is responsible for ROS counterbalance in diverse metabolic routes [26]. The major metabolic activity in cancer cells provokes an overexpression of GSH (up to mM [27]) and a larger dependency of their levels. Therefore, the inhibition of GSH synthesis or its direct removal through catalytic processes [22] guarantees a ROS disruption in the cell leading to its apoptosis. Finally, it has been recently demonstrated that the generation of H_2 inside a tumor cell may induce a disruption of the mitochondria, causing a disarrangement in ATP levels (Figure 2).

Noble metals have also attracted great attention in multiple biomedical applications due to their unique properties in terms of biocompatibility, stability and optical response [28–30]. A wide variety of applications have been demonstrated for noble metals to act as optimal nanoagents to selectively enhance well-established or developed therapies. It has been shown how metal-based nanomaterials can improve radiotherapy (RT) [31], sonodynamic therapy (SDT) [32] or electrodynamic therapy (EDT) [33]. Smart nanoplateforms have been designed to effectively respond to the tumor microenvironment (TME), simulate enzyme properties [34,35], act as drug delivery systems [36] or as immunonano-carriers [37], perform starvation therapy (ST) [38] or activate designed prodrugs to perform in vivo biorthogonal catalysis [39,40]. In addition, light-induced therapies have been also taken advantage of noble metal nanoparticles to selectively enhance therapy performance. In the last few years, noble metal-based nanoparticles have risen as one of the most promising

alternatives to selectively promote light-triggered therapies such as photothermal therapy (PTT) [41,42] or PDT [43].

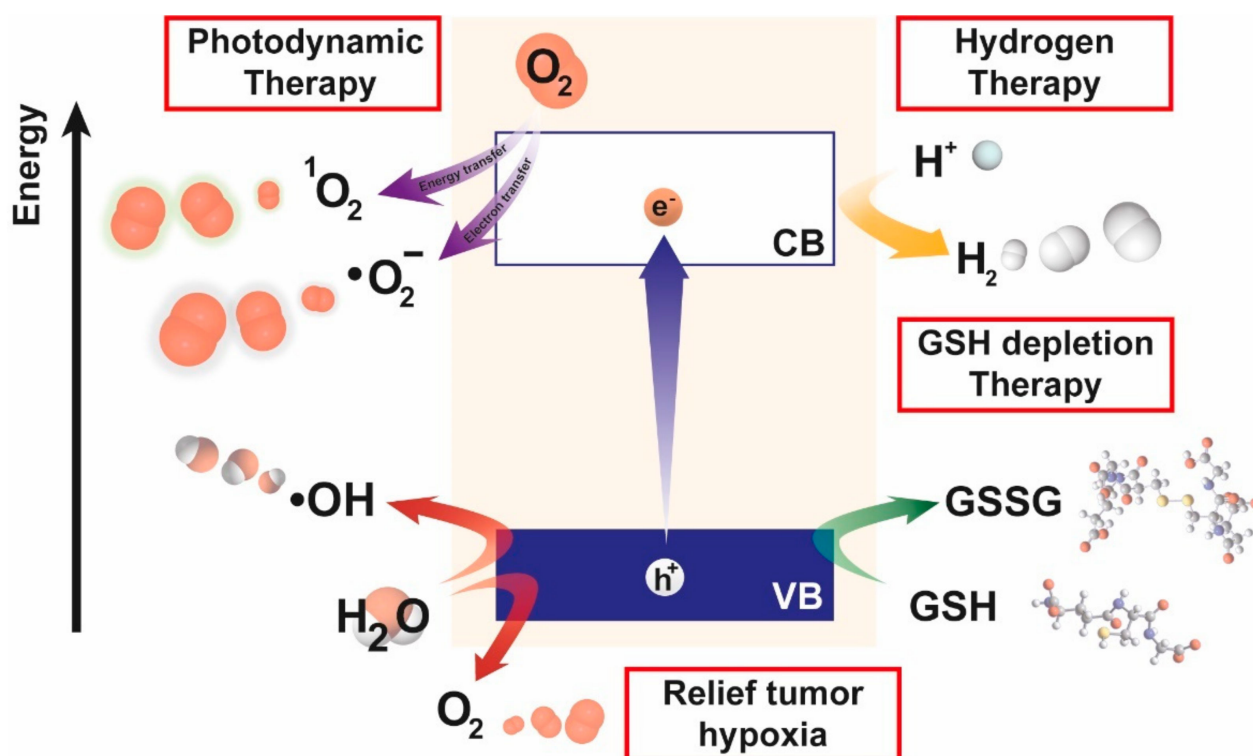


Figure 2. Photocatalytic reactions performed by nanostructured catalysts of interest for cancer therapy. Most of these photocatalysts are reported to produce ROS (i.e., $^1\text{O}_2$, $\bullet\text{OH}$ and $\bullet\text{O}_2^-$), but recent works endorse these photocatalysts the capability to generate H_2 or O_2 through the reaction of aqueous H^+ with photogenerated e^- and the consumption of photogenerated h^+ by H_2O molecules, respectively. Moreover, some photocatalysts may also transform intracellular GSH into GSSG via h^+ consumption. These reactions are added to the toolbox employed by photocatalysts to achieve a more efficient cancer therapy.

This review focuses on the different engineering strategies adopted in recent years to enhance the photocatalytic response of nanoparticles for cancer therapy. We tackle the most recent efforts to improve the local O_2 supply in tumor environments, the elimination of GSH to maximize the action of ROS species and overall, we emphasize the role of different photocatalysts beyond organic PSs working on PDT. We overview the exploited approaches to engineer active photocatalysts including: (1) the design of narrow E_g photocatalysts; (2) using noble-metal based nanostructures; (3) the combination of different photocatalyst to create diverse heterojunctions (type-II heterojunctions, Z-schemes and metal-semiconductor heterojunctions).

2. Use of Low Energy Bandgap Photocatalysts

Classical semiconductor photocatalysts such as ZnO or TiO_2 are highly efficient to induce ROS generation in aqueous media [44], but their large E_g (3.4 and 3.2 eV [45], respectively) limits their application in PDT. In addition, when the particle size decreases down to few nanometers, the resulting E_g of the nanomaterial tends to be wider. The quantum confinement of the electrons present in the nanoparticle induces an energy shift of the VB and CB levels towards more positive and negative potentials, respectively [46]. In the recent years, there have been multiple attempts to obtain novel photocatalysts with suitable E_g as alternatives for PDT application (Table 1).

Table 1. Different photocatalytic materials with low E_g applied for PDT.

Material	Measured Band Gap (E_g) (eV)	Light Irradiation (nm)	Catalysis Products	Reference
BP NSs ^a	2.0	660	1O_2	[47]
MoS ₂ QDs	1.875	630	$\bullet O_2^-$	[48]
Cs _x WO ₃ NRs		880 + 1064	1O_2	[49]
BP QDs ^b		625 + 880	1O_2	[50]
RPCN ^c	1.71	808	GSSG, H ₂	[51]
TiSe ₂	1.77	808	GSSG, $\bullet O_2^-$, $\bullet OH$	[52]
B-TiO ₂	-	808	$\bullet OH$, 1O_2	[53]
G-TiO ₂	-	980	$\bullet OH$, 1O_2	[54]
C ₅ N ₂ NPs	1.63	650 + 808	O ₂ , 1O_2	[21]
g-C ₃ N ₄ -GOx ^d	2.30	630	O ₂	[55]
SWCN ^e	-	808	$\bullet O_2^-$, 1O_2	[56]
Nanographene	-	980	1O_2	[57]
C ₆₀ -IONP ^f	-	532	ROS	[58]
N-CDs	-	740	H ₂ O ₂ , $\bullet O_2^-$	[59]
N-CDs-TPP ^g	-	625	1O_2	[60]
Zr-FeP	-	635	1O_2	[61]
TCPC-UiO ^h	-	635	1O_2	[62]
W ₂ C	0	1064	$\bullet OH$, 1O_2	[63]
Mo ₂ C	0	808	$\bullet OH$, O ₂	[64]

^a Black Phosphorous Nanosheets; ^b Quantum Dots; ^c Red Polymeric Carbon Nitride; ^d Glucose oxidase; ^e Single Walled Carbon Nanotube; ^f Iron Oxide Nanoparticle; ^g Mono-hydroxyphenyl triphenylporphyrin; ^h Tetratopic Chlorin-Universitetet i Oslo.

2.1. Nanostructured Inorganic Photocatalysts

Black phosphorous (BP) represents one of the first examples of a nanostructured inorganic photocatalyst applied to PDT [47,50,65]. Controlling the dimensions and morphology of BP enables the correct matching of the incident irradiation source (suitable for a biocompatible window) with the tunable E_g . BP can vary its E_g from 0.3 eV (in bulk) to a 2.0 eV for a BP monolayer [66]. Wang et al. [47] demonstrated the capability of BP nanosheets to yield 1O_2 from O₂ using a 660 nm laser in human MDA-MB-231 breast cancer cells. In vivo results also showed the photocatalytic activity of BP and its efficacy inhibiting tumor growth with a combination of 660 nm irradiation and a dose of BP of 0.6 mg/kg (Figure 3a). BP QDs have also been successfully applied to the photocatalytic conversion of O₂ into 1O_2 for PDT [50], using a combination of 625 and 808 nm light. Both BP nanostructures, NSs and QDs, displayed good biocompatibility in vivo [47,50]. Although classical TiO₂ is not suitable for PDT due its narrow E_g , it can be chemically modified to allow the use of biocompatible irradiation to perform photocatalysis. The Shi group [53] developed black-TiO₂ (B-TiO₂) starting from P25 nanoparticles through the reduction of TiO₂ using aluminum at low temperature. In another study, they also prepared green-TiO₂ (G-TiO₂) nanoparticles by applying an ultrasonication process to B-TiO₂ [54]. Both materials demonstrate an encouraging PDT capability under 808 and 980 nm for B-TiO₂ and G-TiO₂, respectively (Figure 3b). Photocatalysts with a metallic-like electronic band structure (i.e., E_g close to 0) have also been evaluated for PDT [63,64]. Li et al. [63] developed W₂C nanoparticles, synthesized the calcination at 800 °C of an organic-inorganic hybrid structure consisting in WO₄⁻ subunits coordinated to polydopamine nanoparticles. Their resulting metallic-like

behavior could achieve photocatalysis under 1064 nm irradiation light due to the creation of e^-/h^+ pairs via interband transitions [67]. The photo-generated charges could produce $\bullet\text{OH}$ and $^1\text{O}_2$ species, detected by electron paramagnetic resonance (EPR) (Figure 3c). ROS were enough to provoke tumor ablation without injuring surrounding organs. Although engineering low E_g photocatalysts entails a precise control of its band structure, size and morphology, the nanosystems developed so far have shown encouraging PDT outcomes results to keep on evaluating NIR-responsive photocatalysts for cancer treatment.

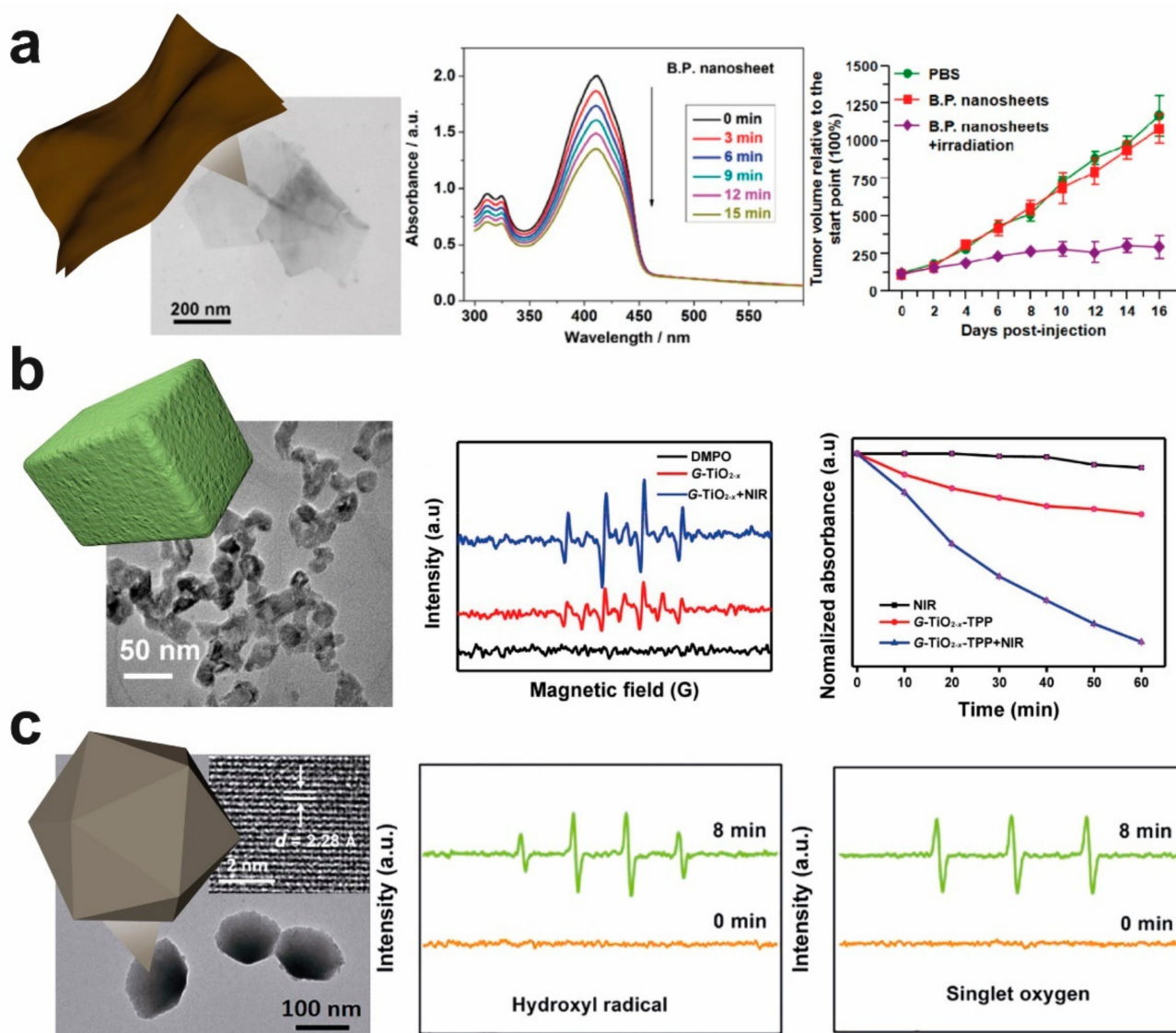


Figure 3. Different low E_g photocatalysts developed for PDT. (a) TEM image of BP nanosheets and evolution of the catalytic conversion of O_2 into $^1\text{O}_2$ under 650 nm light irradiation. Applying those conditions reduced considerably the tumor size in Balb/c mice. Reprinted with permission from [47]. Copyright © 2015 American Chemical Society; (b) TEM image of Green-TiO₂ (G-TiO₂) applied for PDT. EPR experiment demonstrating the capability of G-TiO₂ of generating OH radicals in the presence of 980 nm irradiation. Photocatalytic degradation of 1,3-diphenylisobenzofuran in G-TiO₂/980 nm system indicating ROS generation. Reprinted with permission from [54]. Copyright © Ivyspring International Publisher; (c) TEM image of W₂C nanoparticles together with EPR spectra of $\bullet\text{OH}$ and $^1\text{O}_2$ species after irradiation with 1064 nm, confirming the photoactivity of W₂C nanoparticles towards ROS production. Reprinted with permission from [63]. Copyright © Tsinghua University Press and Springer-Verlag GmbH Germany, part of Springer Nature 2018.

2.2. Carbon-Based Photocatalysts

Engineering suitable E_g has been also successfully explored for carbon-based nanomaterials [21,51]. Different carbon nanostructures have been engineered to achieve the photocatalytic process inside tumor cells, including single-walled carbon nanotubes (SWCN) [56], fullerenes (C_{60}) [58], graphene oxide [57] or carbon dots [68,69]. Xu and co-workers developed a methodology to promote NIR-absorption in C_3N_4 nanoparticles consisting in intercalating K within the C_3N_4 structure [51]. This chemical modification altered the position of CB of C_3N_4 from +1.71 V to +0.71 V, achieving an E_g of 1.71 eV, suitable for photo activation under biocompatible irradiation. Although most developed photocatalysts for PDT focus on the ROS production from photogenerated e^-/h^+ pairs some works have shown the potential of these h^+ to subsequently oxidize key tumor molecules such as GSH. Thus, catalytic GSH depletion is considered a new horizon in cancer therapy research [22]. VB position K-doped- C_3N_4 photocatalyst (0.71 V) allowed the GSH oxidation reaction into GSSG (0.32 V [51]) while CB position (−1.0 V) supported H_2 evolution from H^+ reaction. The majority of classic photocatalysts usually work under ultraviolet-visible (UV-vis) irradiation, which does not penetrate skin and consequently, does not reach tumor sites [3]. Another strategy to mainly activate carbon-photocatalysts inside a tumor consist in the combination of upconverting nanoparticles (UCNP) and photoactive nanostructures. UCNP are able to absorb two photons with low energy (and thus, with large tissue penetrability) and convert them into a more energetic photon, suitable to interact with the VB of a semiconductor [70] and carry out photocatalytic process. g- C_3N_4 is a widely used efficient photocatalyst applied in water splitting, organic transformations or environmental remediation [71]. Its application in PDT has been reported with different morphologies (g- C_3N_4 quantum dots [72,73] or g- C_3N_4 nanosheets [74]) in combination with UCNP, as E_g of g- C_3N_4 value is 2.7 eV (i.e., <475 nm).

These materials also tackled the oxygen scarcity issue associated to the TME [75]. Photogenerated e^- are able to interact with O_2 to form 1O_2 or $\bullet O_2^-$, and consequently the limited supply of O_2 entails a loss of PDT efficiency. Chen et al. [21] developed C_5N_2 nanoparticles with a characteristic VB with a potential of 2.06 V enough to oxidize H_2O into O_2 and overcome the tumoral hypoxia, while generating 1O_2 from the produced O_2 . The major advantage of this system lies in its ability to correct photocatalytic activity despite the hypoxic environment (Figure 4a) inherent to tumor cells. CDs have emerged as outstanding materials to perform diagnosis and therapy as single freestanding platforms [68]. The synthesis of CDs comprises the calcination of an organic molecule [59], generally containing nitrogen to provide the CD of an expanded energy level to provide an enhanced photocatalytic response towards the visible-NIR ranges [76]. In this way, the synthetic versatility and chemical affinity of CDs favors the integration and enhanced interaction with PSs to provide an efficient 1O_2 generation. Likewise, CDs are also able to increase the solubility and stability of PSs, as pointed out by Xie et al. [60]. CDs may also perform PDT on their own [59,69] (Figure 4b) positioning them as promising theragnostic materials. Finally, another smart approach to overcome PSs limitations is the design of metal organic frameworks (MOFs) with PSs integrated (Figure 4c) within their reticular structure [61,62,77]. The catalytic activity of these MOFs yields the same product as in the case of PSs (i.e., 1O_2), but with enhanced stability.

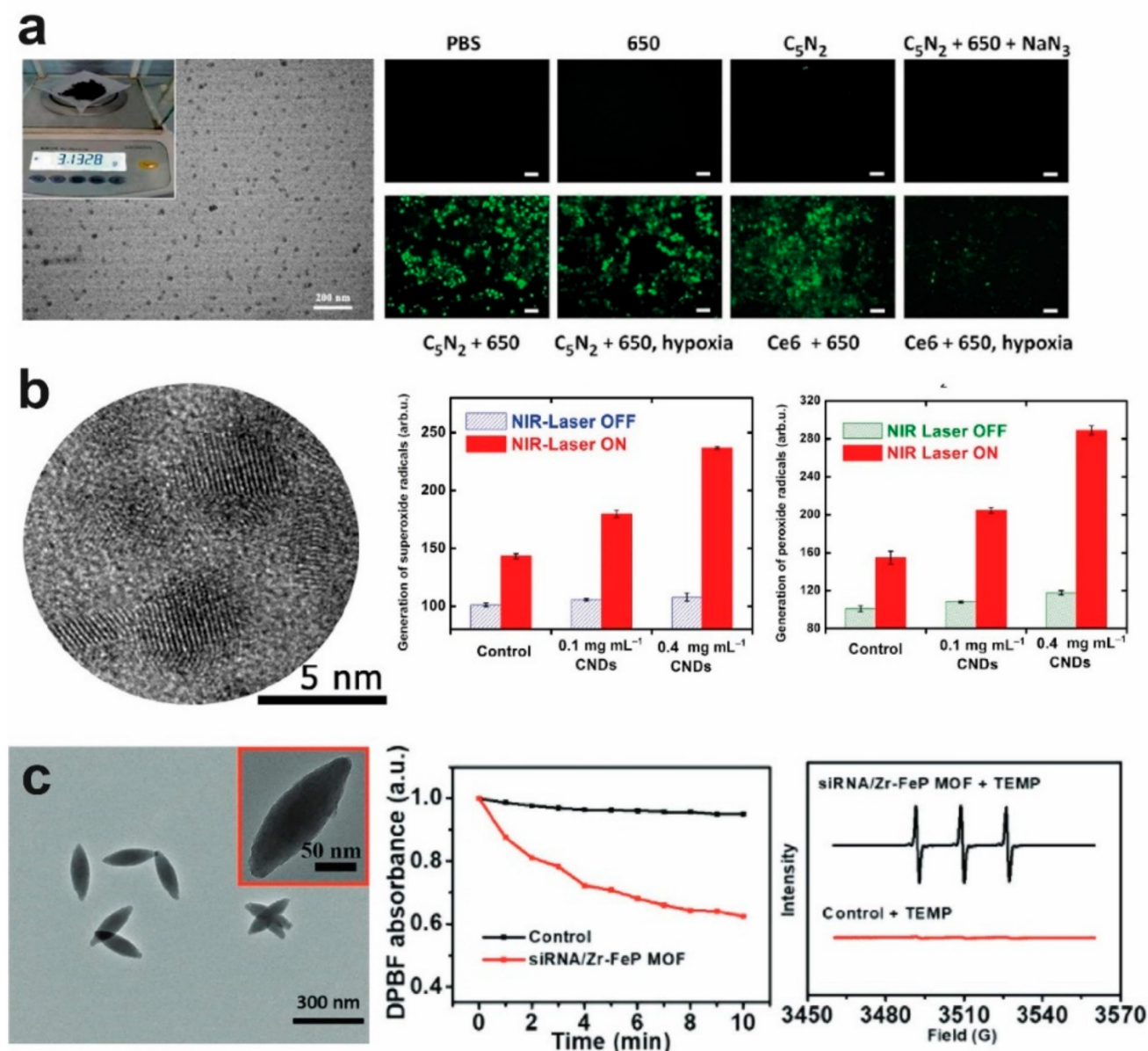


Figure 4. Selection of carbon-based photocatalysts developed for PDT. (a) TEM image of K-doped C₃N₄ nanoparticles applied for PDT. In vitro experiments demonstrate the K-C₃N₄ capability of generate O₂ and ¹O₂ simultaneously under 650 nm light irradiation. Reprinted with permission from [21]. Copyright © 2021 Wiley-VCH GmbH; (b) TEM image of N-doped carbon dots and their in vitro photogeneration of peroxide and superoxide species under NIR irradiation. Reprinted with permission from [59]. Copyright © 2019 Wiley-VCH Verlag GmbH & Co. KGaA, Weinheim; (c) TEM image of zirconium-ferriporphyrin metal organic framework (Zr-FeP MOF). Photocatalytic performance of Zr-FeP MOF generating ¹O₂ demonstrated by DPBF assay and EPR spectroscopy. Reprinted with permission from [63]. Copyright © 2018 WILEY-VCH Verlag GmbH & Co. KGaA, Weinheim.

3. Noble Metal-Based Photocatalysts for Cancer Therapy

3.1. Conjugation of PSs with Noble-Metal Nanoparticles versus Direct O₂ Photoactivation on the Metal Surfaces for PDT

Until very recently, the use of metallic nanoparticles in PDT for cancer therapy had been strictly restricted to PS-bioconjugated metal nanohybrids. Different metal nanoparticles (Au, Pd, Pt) have been bioconjugated with organic PSs such as Chlorine e6 (Ce6) or Indocyanine Green (ICG). Hybrid systems take advantage of physical, optical and cat-

alytic properties of metal NPs to either improve the efficacy of PDT or promote synergistic co-therapies. Pt and Pd nanoparticles are able to catalyze H_2O_2 decomposition to form O_2 , alleviating tumor hypoxia and enhancing better results in O_2 -dependent PDT [78,79]. Moreover, Au-based materials have been also used to perform *two in one* PTT/PDT [80].

One of the first examples of metal nanoparticles use for $^1\text{O}_2$ generation was reported by Kotiaho et al. [81]. Taking advantage of classical organic PS molecules to enhance $^1\text{O}_2$ generation, Au NPs were bioconjugated with thiolated phthalocyanines. It was been demonstrated how phthalocyanine-functionalized Au NPs successfully photo-induced charge and energy transfer between the metal surface and the organic bonded macrocycle. They concluded how a selective excitation of the gold cores in the pump–probe experiment results in an energy transfer from the gold nanoparticles to the attached phthalocyanines in ~ 2.4 ps. Moreover, photoexcitation of the phthalocyanines attached to the functionalized nanoparticles led to an electron transfer to the gold core in ~ 3.0 ps. Therefore, the energy-donating ability of the gold nanoparticles can be used to extend the absorption range of phthalocyanine, and, at the same time, charge separation between phthalocyanines and gold nanoparticles is achieved (Figure 5).

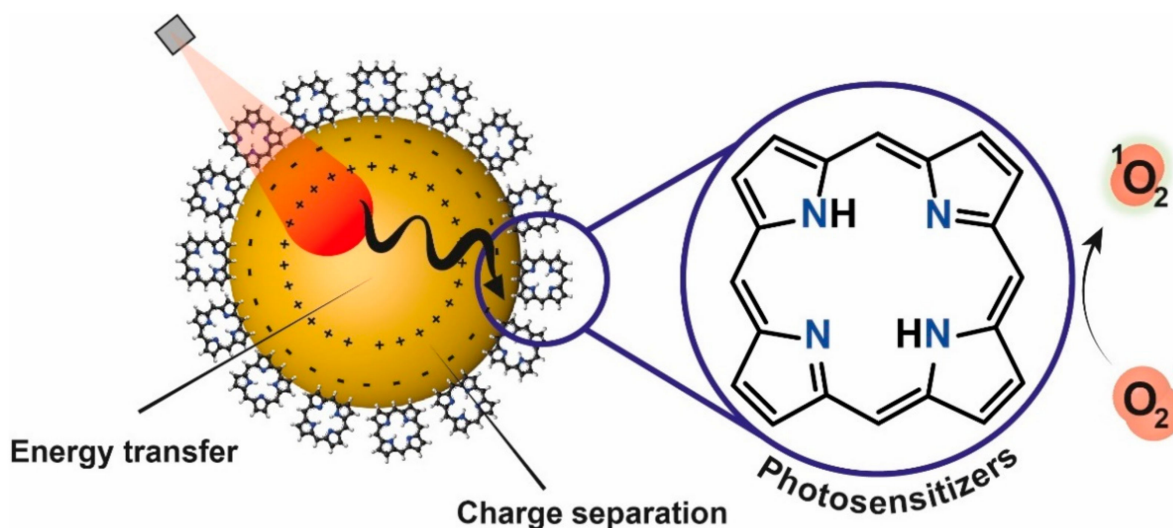


Figure 5. Synergy between phthalocyanines conjugated to noble-metal nanoparticles responsive to biocompatible irradiation. The excitation of e^- own to noble-metal nanoparticles provoke its transference to the organic molecule bonded to the nanostructure surface to transform dissolved O_2 into reactive $^1\text{O}_2$. Moreover, this electronic transference boosts a charge separation between the phthalocyanine and the nanoparticle to enhance the photocatalytic process [81].

3.2. Influence of the Crystalline Facets Exposed to O_2

Less attention has been traditionally paid to selectively promote a photo-induced charge and energy transfer directly between the metal surface and O_2 . Raviraj et al. [43] demonstrated that metallic nanoparticles (Au, Ag, Pt) could selectively generate $^1\text{O}_2$ species without organic sensitizer requirement under irradiation (100 W high-pressure Hg lamp for 2 min). Light-induced O_2 activation takes place after an effective chemisorption onto the surface of the metal nanoparticle. However, O_2 tend to dissociate on the catalytic surface of metals and only keeps the molecular form in the presence of specific crystalline facets of the metal nanocrystals (Figure 6a) [82]. For instance, (111) orientations in Ag nanocrystals preferentially chemisorb molecular O_2 . In contrast, (100) and (110) planes are prone to accommodate the dissociated atomic O species. Only molecular oxygen can be further activated to generate $^1\text{O}_2$ [43,82]. Thus, the irradiation wavelength, the type of metal used, morphology and the type of facets exposed are fundamental parameters to evaluate and predict the suitability and potential of metal nanoparticles as PDT agents.

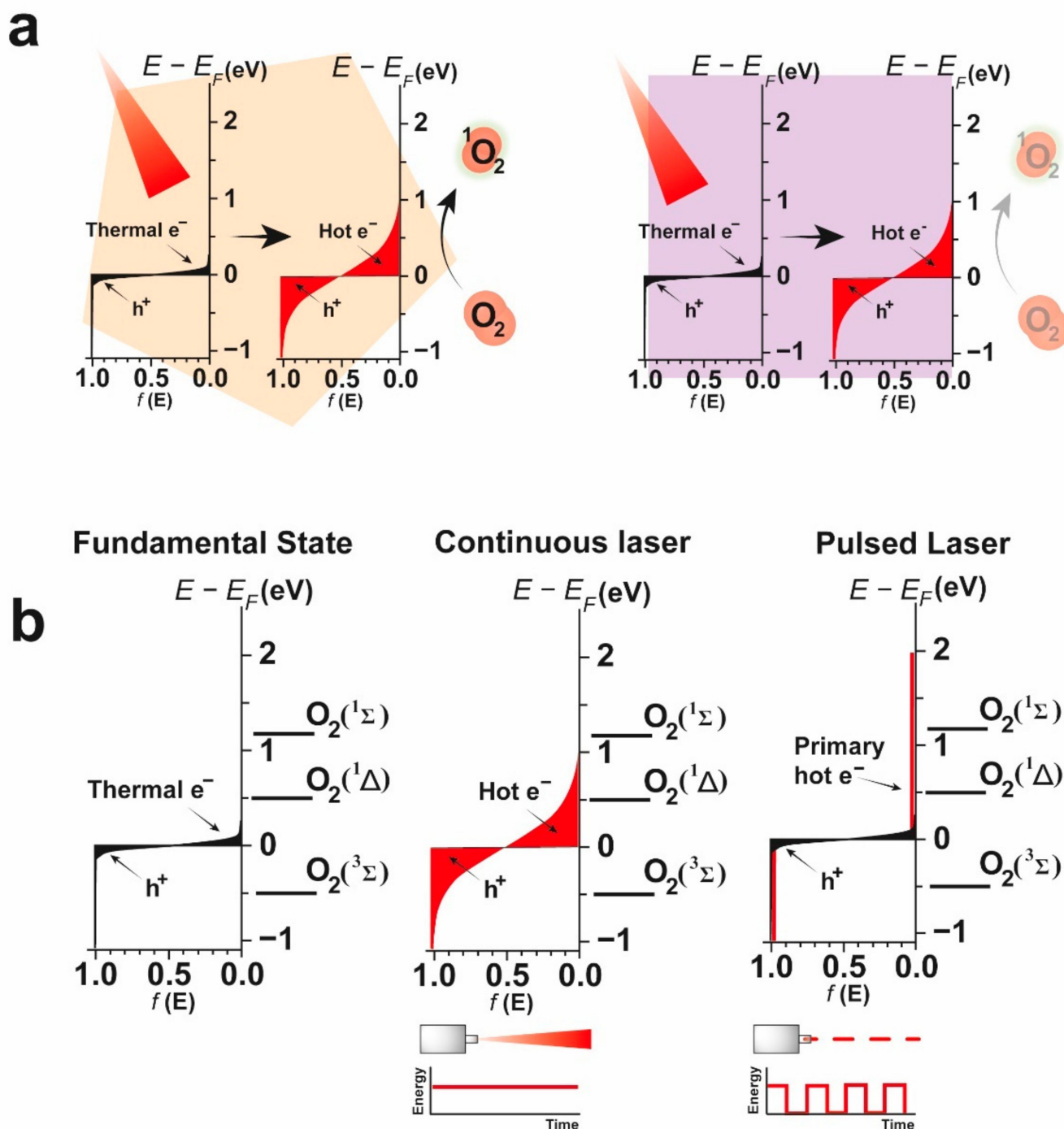


Figure 6. (a) Crystalline-facet dependence in singlet oxygen generation. O_2 stabilization in certain surface facet promote an efficient energy transfer between metal crystals and previous chemisorb O_2 ; (b) Schematic illustration of metal-based photo-excitation under visible and NIR excitation wavelengths. Non-irradiated condition with excited thermal electrons, light irradiation and its subsequent response to generate highly energetic primary hot electron/holes followed by electron/holes equilibrium stabilization as a function of the type of laser used.

3.3. Influence of the Type of Laser Irradiation Source

Pasparakis et al. studied the generation of 1O_2 in culture media when it was incubated with gold nanoparticles (40 nm) under laser irradiation ($\lambda_{exc} = 532$ nm). To investigate the PDT induced cell death mechanism, they performed analogous studies in the presence of 1O_2 scavengers such as ascorbic acid (AA) or 1,3-diphenylisobenzofuran (DPBF). When

AA or DPBF were co-incubated, cell death was dramatically reduced, thereby indicating that in their case, Au NPs were inducing cell death using $^1\text{O}_2$ as the dominating and more abundant ROS. Moreover, they studied the influence of the laser sources and tested continuous wave (CW) ($50 \text{ mW}/\text{cm}^2$ for 20 s) and pulsed laser irradiation (30 mJ/cm^2 ·pulse, 33 pulses with 10 Hz repetition rate) modes. Their results showed a higher fraction of $^1\text{O}_2$ when pulsed laser irradiation was applied [83]. Variations in cell viability were attributed to differences in the laser-induced activation pathways. CW irradiation induced an activation mechanism enabled by the interaction of plasmons and hot electrons with molecular O_2 , and an indirect photothermal pathway.

The pulsed laser source may also induce extreme heat leading to a potential particle fragmentation and increased thermionic electron emission (Figure 6b). Chadwick et al. [84] studied the influence of the variation of metal nanoparticle size to generate singlet oxygen under laser irradiation ($\lambda_{\text{exc}} = 532 \text{ nm}$ either with CW or pulsed laser irradiation). They evaluated citrate capped gold nanoparticles of 15 and 46 nm and they found a greater ability of the larger Au NPs to form singlet oxygen species. They attributed a higher capacity of bigger gold nanoparticles to generate more hot electrons compared with small ones. Moreover, they carried out a systematic comparison between both, CW and pulsed laser irradiation. Pulsed laser irradiation acted via the equilibrated hot electrons, reaching temperatures of several thousand degrees during each laser pulse. CW can act only via the directly excited primary hot electrons, losing energy by electron-electron equilibration and consequently minimizing $^1\text{O}_2$ generation under analogous conditions (Figure 6b).

3.4. Influence of the Shape, Morphology and Aggregation State of the Nanoparticles

The influence of shape and morphology was systematically investigated by Zhao et al. [85]. They carried out experiments irradiating Au nanorods (Au NRs) with different aspect ratios with a two-photon laser source (808 nm with an energy density of 3.0 W cm^{-2}). Au NRs (maximum absorbance band at 765, 808 and 835 nm) were compared with other representative organic singlet oxygen sensitizers such as ICG or Rose Bengal (RB). As a result, $^1\text{O}_2$ generation efficiencies were enhanced in the presence of Au NRs under two-photon laser irradiation. Moreover, Au NRs with a maximum absorbance at 808 nm exhibited a better performance towards $^1\text{O}_2$ generation than those with maxima absorbance bands centered at 765 and 835 nm. The high efficiency of Au NRs for PDT with two-photon laser irradiation was not observed with a one-photon excitation source.

Jiang et al. also evaluated the influence of the aggregation state of Au NPs and Au NRs to promote $^1\text{O}_2$ generation [86]. They reported a dramatically enhanced ROS generation when both nanospheres and nanorods were aggregated. They realized that aggregated spherical Au NPs and short Au NRs enhanced ROS generation. In contrast, aggregation in longer Au NRs did not promote a significant increment in ROS generation values.

It has been shown how aggregated Au NPs expand their absorbance toward higher wavelength values than their isolated counterparts [87]. Jiang et al. [86]. performed singlet oxygen generation experiments under 800 nm laser irradiation conditions (beam area = 0.3 cm^2 , pulse duration of 60 fs and repetition rate of 1 kHz and energy power density of 3.0 Wcm^{-2}). LPR of Au NPs and short Au NRs are located around 500 and 700 nm respectively. However, LPR of longer Au NRs is located around 800 nm. Cysteine addition tends to aggregate gold nanostructures and shift the maximum plasmon peak of Au NPs and short Au NRs from lower wavelength to around 800 nm wavelength, generating gold-based structures with a maximum peak around the irradiation wavelength used.

Au nanostructures in general, tend to aggregate inside cells. There are several reasons why Au NPs can aggregate. Albanese et al. [88] discussed the influence of NaCl to neutralize the stabilizing electrostatic forces on the citrate-capped Au NPs and cause the van der Waals forces to drive aggregation. Yang et al. [89] also evaluated intracellular Au NPs aggregation and their potential application in PDT. They synthesized Au NPs with different surface charge and performed a co-incubation of both positive and negative gold nanoparticles to

promote a further intracellular aggregation. Gold nanoaggregates performed better results in terms of $^1\text{O}_2$ generation compared with non-aggregated gold nanoparticles.

Vankaya et al. [90] evaluated the one-photon laser irradiation of Au NRs and its photocatalytic oxygen activation for $^1\text{O}_2$ generation. They performed *in vitro* and *in vivo* experiments using polymer coated Au NRs to enhance PTT and PDT. They tested irradiation wavelengths in the visible (550 nm) and NIR (940 nm) windows to significantly reduce HeLa cell viability. They confirmed that the irradiation at 550 nm induced killing of HeLa cells by a photothermal effect. HSP 70 is considered the most sensitive biological indicator for thermal shocking stress. Upon 550 nm laser irradiation, HSP 70 levels were considerable higher than blank experiments, as well as 940 nm laser irradiation experiments. Moreover, experiments performed at 4 °C confirmed photothermal effect of Au NRs by significantly suppressed HSP 70 overproduction. On the other hand, death mechanism of HeLa cells upon 940 nm laser irradiation mainly turned on a ROS-mediated PDT. Experiments carried out under 940 nm laser irradiation at 37 °C and 4 °C showed no significant increase of HSP 70. Likewise, experiments performed at reduced temperature were able to generate a major fraction of ROS in comparison with the analogous experiments at 37 °C. To confirm ROS-mediated cell death mechanism, cells were pretreated with NaN_3 , a well-known ROS inhibitor, that confirmed the lower ROS production levels at both reaction temperatures. Furthermore, *in vivo* studies were also performed under 780 nm and 915 nm laser irradiation wavelength with identical outcome. Enhanced ROS generation were obtained under 915 nm laser irradiation, thereby indicating the need to select the proper NIR irradiation source to match the coupling with the nanometals and maximize the penetration depth.

Vijayaraghavan et al. [91] also explored a different nanometallic photocatalyst design based on multi-branched Au nanourchins (Au NUs) for PTT and PDT activated in the first and second biological window (Figure 7a–c). They synthesized a polymer-coated Au-based multibranching nanoarchitecture with expanded NIR absorption towards the first and second window. Analogous studies were analyzed at 4 °C and 37 °C and in the presence/absence of the NaN_3 scavenger and similar results were obtained (Figure 7d). Moreover, taking advantage of its expanded absorption properties, Au NUs were evaluated to selectively perform PTT/PDT at different wavelengths. $^1\text{O}_2$ generation for Au NUs was evaluated under 550 nm and 808 nm (CW lasers at 130 mW/cm² power intensity for 10 min) laser irradiation wavelengths and no significant results were obtained. In contrast, 915 nm and 1064 nm NIR sources selectively enhanced $^1\text{O}_2$ generation with the Au NUs (Figure 7e,f). The authors attributed the selective tendency to either PTT or PDT to the unprecedented architecture of the Au NUs. It has been shown how Au NRs are active when they were irradiated under first biological window (915 nm) but not when second biological window was used (1064 nm). However, Au NUs showed a remarkable activity in both the first and second biological windows, respectively [91]. To further clarifying the influence of wavelength used and its PDT response, fluorescence experiments were performed and different excitation wavelength-dependent response were monitored. The quantum yields for sensitization of singlet oxygen by Au NUs were considerable higher than obtained for conventional organic photosensitizer or UCNPs sensitized organic photosensitizer under NIR light irradiation [92].

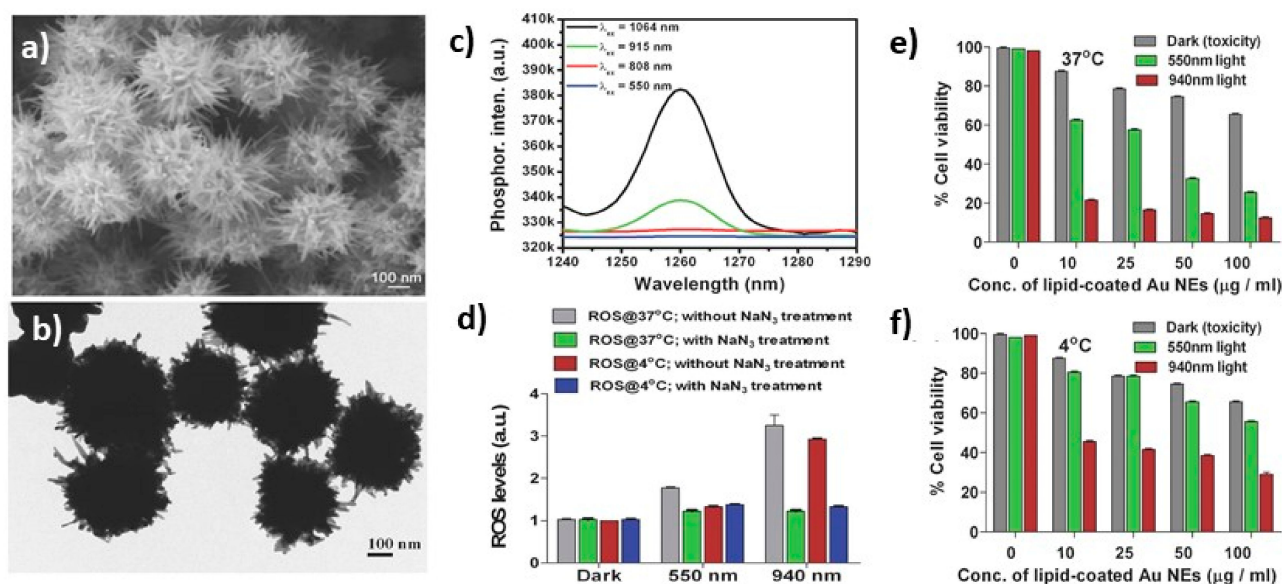


Figure 7. Several examples of gold-based nanoarchitectures with light-induced features to promote PDT and selectively enhance in vitro and in vivo cancer therapy. (a) Scanning electron microscope (SEM) and (b) TEM images for Au NUs; (c) $^1\text{O}_2$ phosphorescence emission spectra sensitized by lipid-coated Au NUs at 550, 808, 915, 1064 nm excitation wavelengths; (d) In vitro ROS generation monitored by the mean DCF fluorescence using flow cytometry for lipid-coated Au NUs internalized HeLa cells followed by photo-irradiation with and without NaN_3 pretreatment, (e) cell viabilities of lipid-coated Au NUs internalized HeLa cells under dark and photoirradiation at 37 °C and (f) 4 °C. Reprinted with permission from [91]. Copyright © 2014 WILEY-VCH Verlag GmbH & Co. KGaA, Weinheim.

3.5. PDT with Other Noble Metal Nanocatalysts beyond Gold

Although less exploited, it is also worth mentioning that other noble metals beyond Au have been successfully reported in the recent literature as alternative photocatalysts able to perform PDT or another co-adjuvant therapy treatment (Table 2, *vide infra*). Pd and Pt nanoparticles have been widely used to selectively bioconjugate organic photosensitizers and perform PDT [35,38]. However, there are fewer examples where these metals have been used in the organic PSs to efficiently enhance PDT for cancer treatment. Li et al. [93] developed novel biodegradable holey palladium nanosheets (Pd NSs) with intrinsic photocatalytic and hypoxia-resistant capacities (Figure 8). For the first time, they fabricated Pd nanosheets with an anisotropic oxidative etching strategy which introduces one-dimensional nanoholes with active (100) facets on the hole walls. $^1\text{O}_2$ photocatalytic activity was tested by EPR. Hypoxia-resistant capacities were evaluated by adding H_2O_2 and monitoring O_2 generation. $^1\text{O}_2$ generation were performed under 808 nm laser irradiation (1 W cm^{-2}) and modified Pd nanosheets (H-PdNSs) showed better yields compared with analogous non modified PdNSs. Moreover, H_2O_2 addition promoted higher efficiency for $^1\text{O}_2$ formation compared with control experiments without H_2O_2 addition. It was explained how H-PdNSs have new exposed planes (100) and how O_2 is more favorable to chemisorb in (100) planes compared with other more relevant planes in non-modified PdNSs. 4T1 cells were incubated with H-PdNSs and irradiated with NIR (808 nm laser with a power density of 1 W cm^{-2} for 3 min) showed greater therapeutic efficacy than non-modified Pd NSs, which could be attributed to the outstanding PDT performance. In order to investigate the hypoxia modulation ability of H-Pd NSs in vitro, H-Pd NSs was tested under both normoxic and hypoxic conditions. The results showed that the cancer cell killing efficiency of H-Pd NSs showed no obvious differences between normoxia and hypoxia, meanwhile, PdNSs showed higher differences between both normoxia and hypoxia experiments.

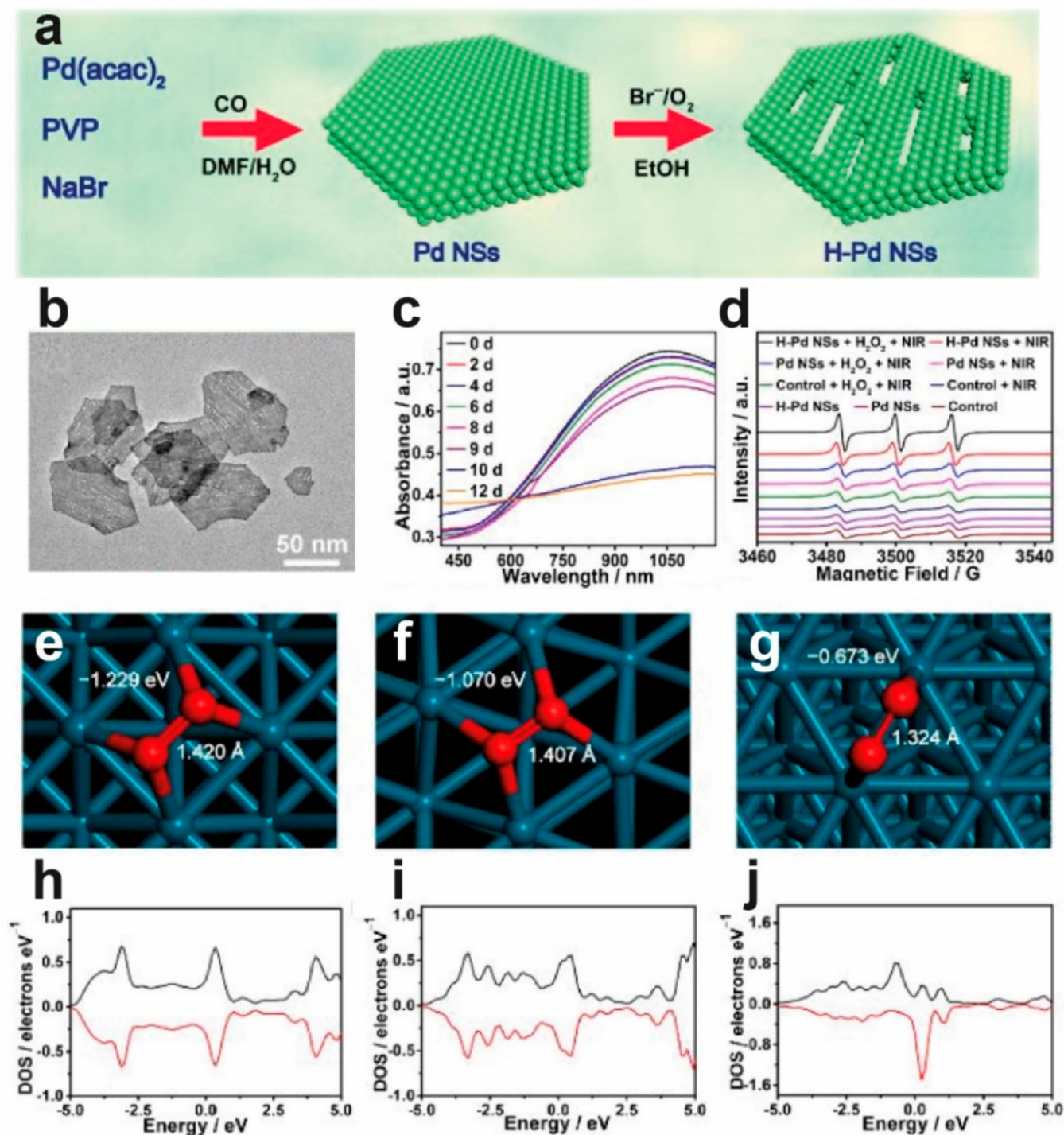


Figure 8. (a) Schematic illustration of the synthetic process for the H-Pd NSs, (b) TEM images of Pd NSs, (c) Etching process of Pd NSs during the first 12 days, (d) EPR spectra of Pd NSs and H-Pd NSs under different conditions (2 W cm^{-2} for NIR groups). The most favorable adsorption configurations of O₂ on (e) Pd(100), (f) Pd(110) and (g) Pd(111) facets. Projected density of states (PDOS) of O₂ on the (h) Pd(100), (i) Pd(110) and (j) Pd(111) facets. Reprinted with permission from [93] Copyright © 2020 American Chemical Society.

Table 2. Noble-metal nanoparticles with photocatalytic activity using light irradiation in the biological window of interest for PDT.

Material	Light Irradiation	Catalysis Product	Reference
Au NPs	532 nm	$^1\text{O}_2$	[83]
Au NRs	765/808/835 nm	$^1\text{O}_2$	[85]
Au NRs/Au NPs	800 nm	$^1\text{O}_2$	[86]
Au NPs	Halogen lamp	$^1\text{O}_2$	[89]
Au NRs	915/940 nm	$^1\text{O}_2$	[90]
Au NUs	915/940/1064 nm	$^1\text{O}_2$	[91]
Pd NSs	808 nm	$^1\text{O}_2/\cdot\text{OH}$	[93]
Au NCs	980 nm	$^1\text{O}_2$	[94]
Au NCs	1064 nm	$^1\text{O}_2$	[95]
Ag NCs	White Light	$^1\text{O}_2$	[96]
AuPd	808/1064 nm	O_2	[97]
AuPt	808 nm	$\cdot\text{OH}$	[98]
Au NCs	808 nm	$^1\text{O}_2$	[99]

3.6. Photocatalytic Activity of Noble-Metal Clusters for PDT

It has been shown how nanoparticles, particularly Au-based NPs, can selectively act as optimal inorganic photosensitizers to enhance PDT upon one and two photon irradiation and how shape and sizes affect to the capacity to selectively generate $^1\text{O}_2$. However, gold nanoclusters (Au NCs) have been also tested as good photosensitizers to selectively promote ROS generation (Table 2). Au NCs have attracted considerable attention in biomedicine due to their biocompatibility and optical and molecule-like properties. They have size dependent optical properties with discrete electronic states which is comparable to the Fermi wavelength of conduction electrons (Figure 9) In 2009, Sakamoto et al. [100] employed single molecule fluorescence spectroscopy to study the correlation between size and photo-reactivity. Small gold nanoclusters ($n < 12$ or 17) fluorescence was significantly quenched by O_2 through an electron transfer mechanism [100]. However, the fluorescence intensity of bigger clusters (m , 19 or 21) increased with higher concentrations of O_2 thereby revealing the great relevance of Au NCs dimensions for photocatalytic applications. Other studies highlight the importance of surface facets in Au NCs to efficiently enhance $^1\text{O}_2$ generation [101]. Bovine Serum Albumin (BSA) capped Au NCs with different facets exposed for O_2 accommodation showed different ratios for $^1\text{O}_2$ generation. O_2 orientation in Au NCs ended up being a key parameter to enhance the PDT process. Highly active nanoclusters had a superoxol-type of O_2 orientation. In contrast, the least active nanoclusters with quenched fluorescence showed a peroxo O_2 orientation. They tested smaller cluster with O_2 vertical adsorption (superoxo) and bigger size gold nanoclusters with peroxo-like O_2 adsorption domains. Theoretical studies support the idea of controlling superoxo and peroxo-like O_2 adsorption domains in smaller and bigger gold nanoclusters. The superoxo-like orientation of the smaller Au NCs leads to retaining of the identity of molecular oxygen and generates singlet states to enhance fluorescence. However, bigger Au NCs with peroxo-like orientation of O_2 is likely to facilitate its dissociation to yield O radicals that initiate the oxidation of the Au-S bonds between protein scaffolds and the encapsulated Au NCs to form bigger Au nanoparticles that may lead to fluorescence quenching.

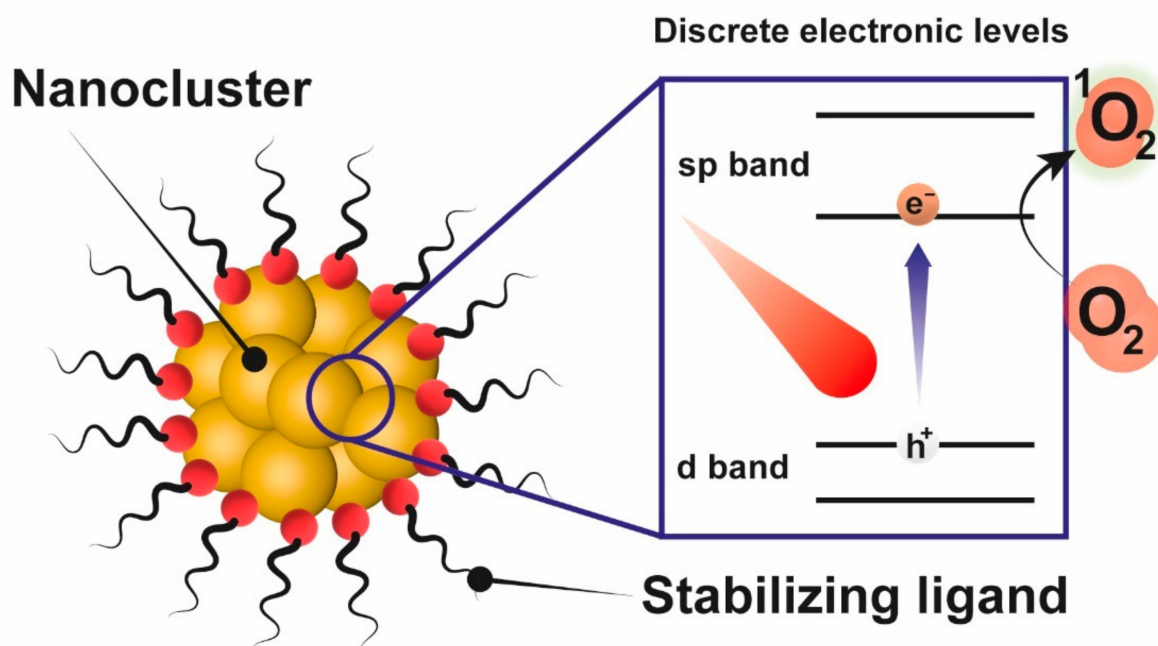


Figure 9. Noble-metal nanocluster stabilized by ligands and its electronic structure composed by discrete levels. The photoexcitation of the electrons present in d band entails an energetic transference to dissolved O_2 to promote 1O_2 generation [102].

There has been great interest in novel design of complex metal-based nanoarchitectures in the last few years [103,104]. Several approaches have been developed to generate advanced hybrid-based structures with synergistic properties. It is well known that one of the most powerful strategies to induce cell death under 1O_2 generation is to target DNA [105,106]. Guanine nitrogen base can be further oxidized by 1O_2 to generate genotoxicity and induce cell apoptosis. Vankayala et al. [94] developed a unique design of nucleus-targeting multifunctional Au NCs to generate singlet oxygen toxic species under NIR irradiation to enhance PDT. Nucleus-targeting peptide (TAT peptide) capped Au NCs (TAT peptide-Au NCs) can selectively reach nucleus cell and successfully induce PDT under NIR light irradiation with O_2 available to efficiently destruct cancer cells without the co-presence of any organic photosensitizer. Confocal fluorescence images revealed the peptide induced selective targeting of HeLa cell nucleus and 1O_2 generation under NIR laser irradiation (980 nm CW laser with a power intensity of 1 W cm^{-2} for 5 min).

Chen et al. [95] developed protein capped Au NCs to enhance PDT under NIR-II irradiation (Figure 10a,b). They used human serum albumin protein (HSA) and catalase enzymes (CAT) as capped proteins to design multifunctional gold-based nanoplatforms (Figure 10a,b). CAT enzymes can selectively react with H_2O_2 to form O_2 , alleviating tumor hypoxia and promoting 1O_2 generation in hypoxic areas (Figure 10c). It was observed how HSA capped Au NCs did not yield 1O_2 efficiently when H_2O_2 was added. However, HSA/CAT functionalized Au NCs effectively improved 1O_2 generation under irradiation when H_2O_2 was added. The multienzyme organic-inorganic hybrid (i.e., BSA/CAT capped Au NCs) could efficiently induce decomposition of over-expressed H_2O_2 in the tumor microenvironment (TME) to yield O_2 (Figure 10d–g).

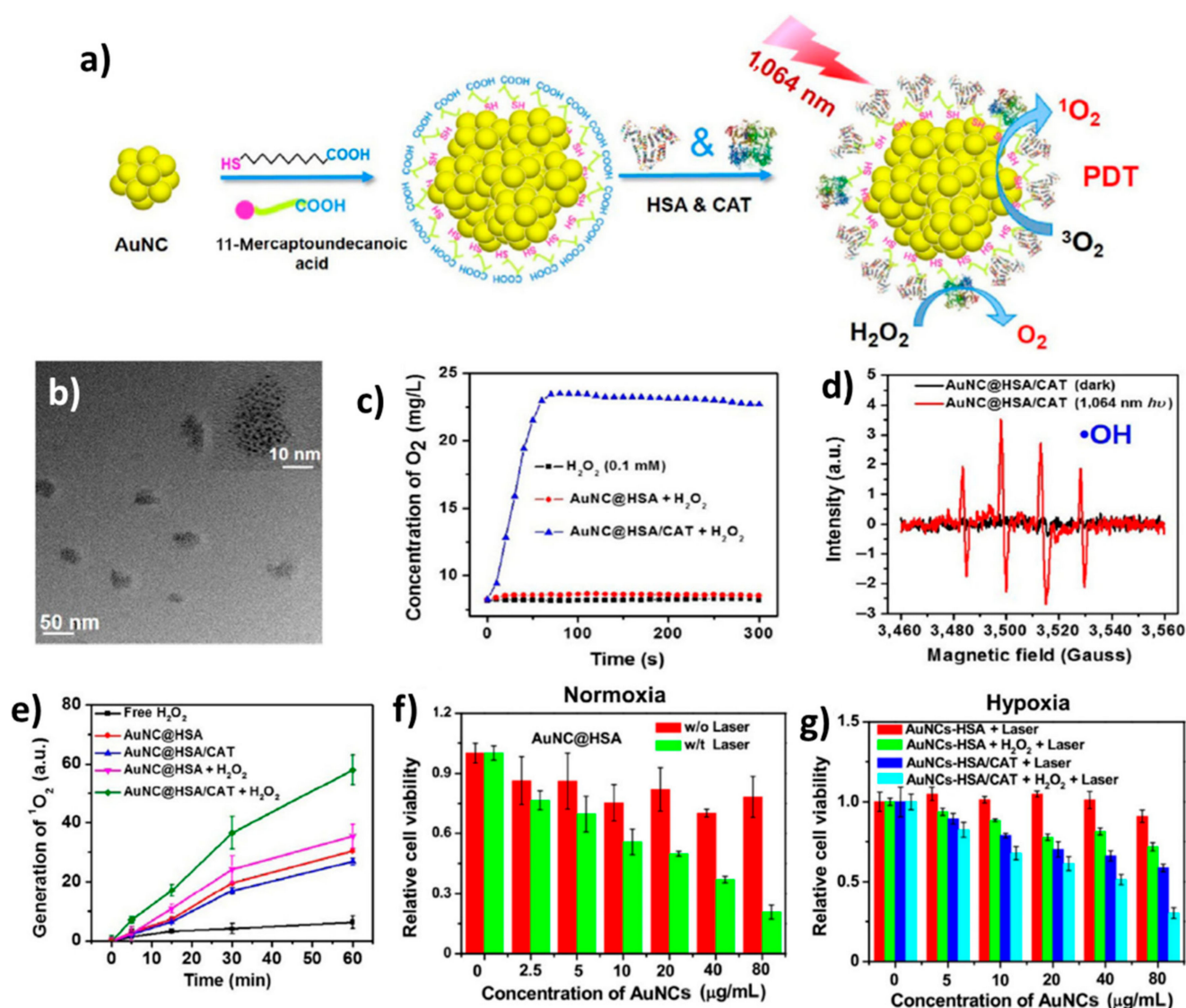


Figure 10. (a) Schematic illustration of the synthesis and synergistic therapeutic effect of Au NC@HSA/CAT nanoparticles; (b) TEM image of Au NC@HSA/CAT nanoparticles; (c) O₂ generation in H₂O₂ solutions (100 µM) incubated with Au NC@HSA or Au NC@HSA/CAT; (d) The generation of •OH determined by EPR spectroscopy to measure DMPO-OH adducts in an aqueous solution containing 0.1 M DMPO; (e) The generation of ¹O₂ determined by the increased SOSG fluorescence, for Au NC@HSA or Au NC@HSA/CAT, with or without addition of H₂O₂; (f) Relative viabilities of 4T1 cells after incubation with Au NC@HSA or Au NC@HSA/CAT with or without the addition of H₂O₂ after 1064-nm laser irradiation (0.2 W cm⁻², 20 min) under the hypoxic conditions; (g) Relative viabilities of 4T1 cells after incubation with Au NC@HSA with or without NIR-II laser irradiation (1064 nm, 0.02 Wcm⁻², 20 min) under the normoxic conditions. Reprinted with permission from [95] Copyright © 2017 Tsinghua University Press and Springer-Verlag GmbH Germany, part of Springer Nature.

Based on a preliminary study, they activated O₂ by Au NCs under light irradiation to form ROS [107]. They confirmed the ROS generation under NIR II light excitation at 1064 nm by EPR spectroscopy. This can be a great treatment advantage given the importance of O₂ for ROS-dependent therapies like PDT in hypoxic tumor ambient.

Although Au NCs have attracted the attention of many researchers in the last few years, Ag nanoclusters (Ag NCs) have also been postulated as a promising alternative to selectively enhance PDT in cancer treatment. Yu et al. [96] developed a BSA-capped

silver nanocluster (BSA-Ag₁₃ NCs) as an effective ¹O₂ generator for PDT upon irradiation with a 150 mW white light source ($\approx 72 \text{ mW cm}^{-2}$). The ¹O₂ generation ability of BSA-Ag₁₃ NCs was evaluated by employing 9,10-anthracenediyl-bis(methylene)dimalonic acid (ABDA) as a chemical probe for ¹O₂ detection. Results confirmed that only BSA-Ag₁₃ could efficiently promote ¹O₂ generation under white light irradiation. Ag ions or AgNPs did not exhibit any photocatalytic response under identical experimental conditions of white light illumination. Moreover, MCF-7 cancer cells were incubated with BSA-Ag₁₃ NCs and about 50% damage cell was achieved with light. The authors attributed this response to a unique energy diagram of the BSA-Ag₁₃ NCs [96]. Upon photoexcitation a small portion (QY of 0.4%) of singly excited electrons underwent radiative relaxation, while a large portion of them transited to triplet states via intersystem crossing. These triplet states were capable of generate ¹O₂ readily with high ¹O₂ generation efficiency.

3.7. Bimetallic Photocatalysts for Cancer Therapy

There exist other relevant reactions where a photocatalytic process can improve the efficacy of other complementary therapies to PDT. The combination of more than one metallic component can be beneficial and synergistic. Photocatalytic decomposition of H₂O₂ to selectively generating molecular oxygen improves O₂ dependence therapies such as radiotherapy. Yang et al. [97] developed a novel Pd@Au nanodisk (ND) with NIR responsive photocatalytic activity. These nanodisks were irradiated with 808 or 1064 nm laser to selectively photocatalyze H₂O₂ to yield O₂. NIR laser irradiation promoted a synergetic photocatalytic reaction to form O₂, alleviating tumor hypoxia and improving O₂ dependent therapies such as radiotherapy (RT). In vivo studies revealed how tumor depletion was dramatically improved when RT was combined with NIR II irradiation, increasing O₂ concentration by photocatalytic reaction of the Pd@Au NDs with H₂O₂. Liu et al. [98] studied the influence of Au@Pt NPs to selectively enhance ROS generation under NIR irradiation. Au@Pt nanoparticles were tested for methylene blue (MB) degradation with/out laser irradiation and H₂O₂. As a result, the MB degradation was enhanced in the presence of Au@Pt NPs in contact with H₂O₂ and irradiated with 808 nm NIR laser.

4. Engineering Heterojunctions to Expand the Photocatalytic Response of Inorganic Semiconductors

A wide range of different low E_g semiconductor and noble metal photocatalysts have been successfully evaluated in vivo for cancer treatments, especially in the context of PDT. Nevertheless, semiconductors usually face an important drawback regarding to charge recombination phenomena [17–19] while the products obtained using noble-metals as photocatalyst are not the most reactive ones (see Table 3). An efficient strategy to enhance charge separation consists in combining different photocatalysts to form a variety of heterostructures: Type-II heterojunctions, Z-schemes and semiconductor-metal heterojunctions. Some photocatalysts based on the construction of heterojunctions applied for PDT are listed in Table 3.

Table 3. Heterojunctions with photocatalytic activity using light irradiation in the biological window of interest for PDT.

Photocatalyst	Heterostructure Type	Measured Band Gap (E_g) (eV)	Light Irradiation	Catalysis Products	Reference
As/As _x O _y	Heterojunction- II	1.4/1.7	660 nm	•O ₂ ⁻ , ¹ O ₂ , GSSG	[108]
BiOI/BiOIO ₃	Heterojunction- II	1.70/3.05	650 nm	O ₂ , •OH, ¹ O ₂	[109]
BiOI/Bi ₂ S ₃	Heterojunction- II	1.63	808 nm	•OH, •O ₂ ⁻	[110]
SbNSs-THPP ¹	Z-scheme	1.75	660 + 808	•O ₂ ⁻ , ¹ O ₂	[111]
Fe ₂ O ₃ -FeS ₂	Z-scheme	2.1/0.90	650 + 808	•O ₂ ⁻ , •OH	[112]
Bi ₂ S ₃ -Bi	Z-scheme	1.41/0.60	808	•O ₂ ⁻ , •OH, O ₂	[113]
g-C ₃ N ₄ -Cu ₃ P	Z-scheme	3.0/1.66	980 (UCNPs)	•O ₂ ⁻ , GSSG, H ₂	[114]
SnS _{1.68} WO _{2.41}	Z-scheme	1.49/2.43	808	GSSG, H ₂	[23]
Ni ₃ S ₂ -Cu _{1.8} S	Z-scheme	1.50/1.47	808	O ₂ , •OH	[115]
Cu ₂ MoS ₄ /Au	Semiconductor/Metal	-	808	•O ₂ ⁻ , •OH	[116]
B-TiO _{2-x} /Au ₂₅	Semiconductor/Metal	1.23	808	•O ₂ ⁻ , •OH	[117]
MoSe ₂ /Au	Semiconductor/Metal	1.52	808	•OH, gluconic acid, H ₂ O ₂	[118]

4.1. Type-II Heterojunctions Applied in Cancer Therapy

Type II-heterojunctions consist in the combination of two semiconductors (denoted as semiconductor I and II), where $E_{CB,I} > E_{CB,II}$ and $E_{VB,I} > E_{VB,II}$ (Figure 11a). After the photogeneration of charge carriers, e^- are transferred to the semiconductor II and h^+ to semiconductor I, achieving a more efficient spatial separation of charges leading to enhanced photocatalysis. The first Type II-heterojunction applied for PDT was reported in 2019 by Zhen et al. [109] with BiOI/BiOIO₃ heterostructures. The band disposition of the BiOI nanostructure allowed the generation of pairs e^-/h^+ under 650 nm irradiation to perform different reactions: photo-generated h^+ are able to produce simultaneously •OH and O₂ from H₂O, while the produced e^- were transferred to BiOIO₃ CB to provoke their reaction with endogenous H₂O₂ to produce •OH. The low dosage necessary to destroy the tumor (0.64 mg/kg) endorse the heterostructure with good biocompatibility. As/As_xO_y have also been successfully applied for PDT as Type II-heterostructures [108] (Figure 11b). In this case, the heterostructure catalyzed GSH oxidation into GSSG using photogenerated As- h^+ , while excited e^- of As were able to transfer their energy to O₂ yielding ¹O₂, or being transferred to CB of As_xO_y to react with O₂ and produce •O₂⁻. The therapy achieved its maximum efficiency combining a 660 nm laser, to perform photocatalytic process, with 808 nm irradiation to produce heat. As/As_xO_y heterostructure exhibited a tendency to accumulate in liver, spleen and lung, but their relatively good biocompatibility and the required low dosage guarantee their biosafety. Although band disposition in type-II heterojunctions boosts charge separation, it also entails an overall decrease of reduction/oxidation potentials of CB/VB of the photocatalyst, respectively.

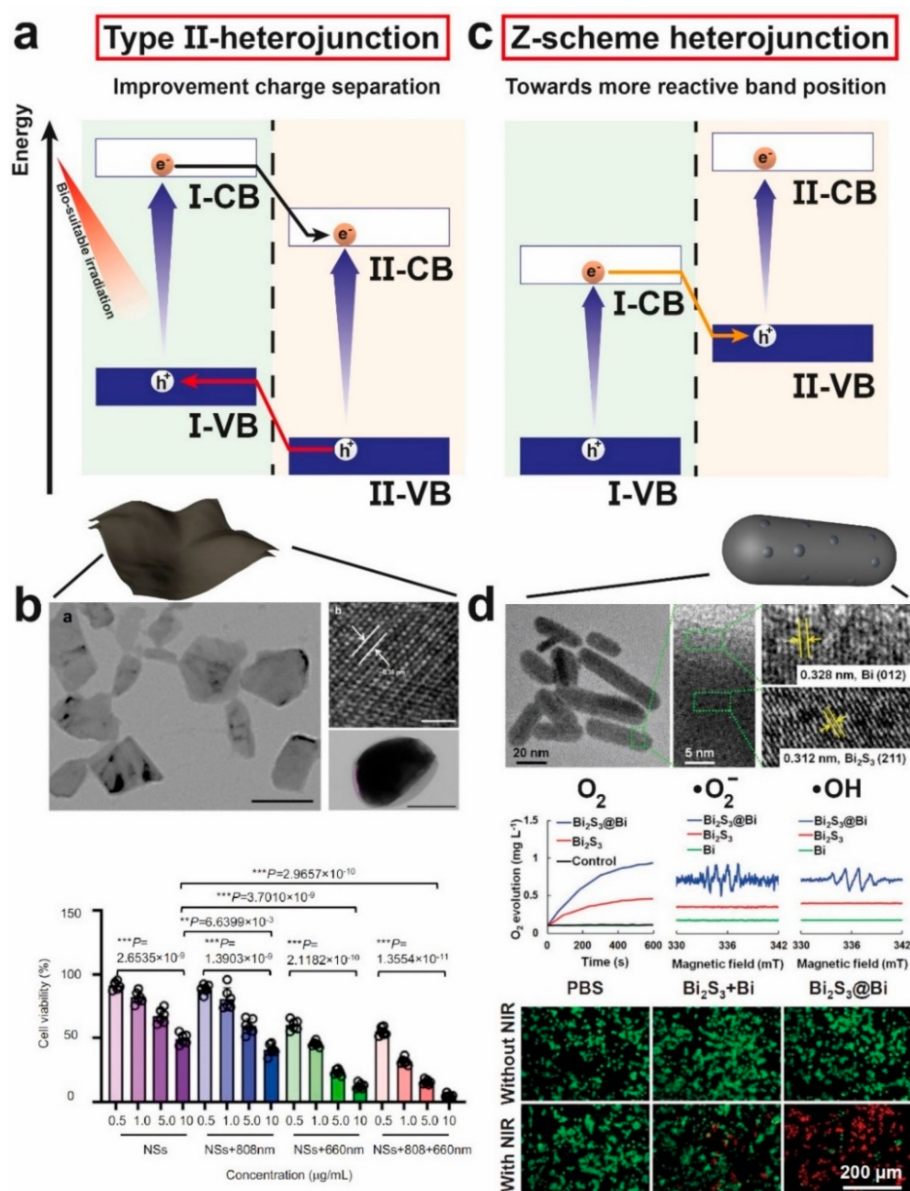


Figure 11. (a) Type-II heterojunction band structure. To boost charge separation and reduce recombination phenomena, band energy is required to be $VB_I > VB_{II}$ and $CB_I > CB_{II}$ to thermodynamically favor the migration of h^+ and e^- to VB_I and CB_{II} , respectively; (b) As/ As_xO_y nanosheets type-II heterojunction applied to PDT. TEM image (scale bar = 100 nm) and HR-TEM (scale bar = 1 nm) of As/ As_xO_y . TEM image (scale bar = 100 nm) of As/ As_xO_y coated with cancer cell membrane nanohybrid. In vitro photocatalytic performance of As/ As_xO_y proving the effectiveness of combining two different light irradiation to perform photocatalysis (660 nm) and photothermal therapy (808 nm). Reprinted with permission from [108]. Copyright © 2021 Springer Nature; (c) Typical Z-scheme band structure, where the energy of each band is ordered following: $VB_I \ll VB_{II}$ and $CB_I \ll CB_{II}$. This band disposition favors the recombination of CB_I electrons and VB_{II} holes, achieving an adequate charge separation while improving band potentials to promote more reactive ROS generation; (d) $Bi_2S_3@Bi$ nanorods (NRs) as Z-scheme applied to PDT. TEM image of Bi_2S_3 NRs decorated with Bi dots. Simultaneous generation of O_2 and ROS (i.e., $\bullet O_2^-$ and $\bullet OH$) under 808 nm irradiation. Live/dead colorimetric test of 4T1 cells under different conditions, proving the efficacy of $Bi_2S_3@Bi$ heterojunction provoking cell death under NIR irradiation. Reprinted with permission from [113]. Copyright © 2020 WILEY-VCH Verlag GmbH & Co. KGaA, Weinheim.

4.2. Use of Z-Scheme Nanostructured Heterojunctions in Cancer Therapy

Z-scheme heterostructures are often explored as an alternative to overcome the type-II heterojunction drawbacks. In these structures, both CB (i.e., CB_I and CB_{II}) are excited simultaneously (Figure 11c). The e⁻ from CB_I are transferred to VB_{II}, leaving stronger reduction/oxidation potentials and thus improving ROS production [112,119,120]. Different Z-scheme configurations have been successfully evaluated for PDT, including Fe₂O₃-FeS₂ [112], SbNSs-THPP (namely, 10,15,20-tetrakis(4-hydroxyphenyl)-21H,12H-porphine) [111], Bi₂S₃-Bi [113], g-C₃N₄-Cu₃P [114], SnS_{1.68}-WO_{2.41} [23] or Ni₃S₂-Cu_{1.8}S [115]. In this case, most of the Z-scheme nanostructures could perform under 808 nm irradiation in comparison with type-II heterostructures, which could work under 650 nm. However, the complexity of biological systems (i.e., different cell lines, tumor models and so on) and the lack of systematic experiments currently prevent a fair comparison among different photocatalysts. Cheng et al. [113] fabricated Bi₂S₃-Bi Z-scheme with different photocatalytic responses (Figure 11d), including O₂, •O₂⁻ and •OH generation under 808 nm irradiation. They highlighted the importance of the contact between photocatalysts in the heterostructure (i.e., Bi₂S₃ and Bi) proving the absence of in vitro and in vivo therapeutic effect when both single-phased materials were introduced simultaneously (Figure 11d). Following the trend found in low E_g photocatalysts and type-II heterostructures, Z-schemes also demonstrate the capability to photooxidize GSH into GSSG, while generating H₂ from H⁺ [23,114]. It has been demonstrated that H₂ (Figure 2) targets mitochondria and may induce cell apoptosis through disruption of cellular energy metabolism by hindering ATP production [121,122].

4.3. Semiconductor-Noble Metal Heterojunctions for PDT

Another widespread strategy to maximize charge separation consists in generating metal-semiconductor heterostructures. Noble metal nanoparticles such as Au possess large work functions (broadly speaking, remove an electron from their surface is a highly energetic process) and thus, they may greatly attract electrons to achieve a successful charge separation (Figure 12a). Lin group [116] demonstrate this concept by fabricating Cu₂MoS₄-Au heterostructure (Figure 12b), which significantly enhanced its photocatalytic activity generating •O₂⁻ and •OH in the presence of Au nanoparticles. Au acted as sinker of the photogenerated e⁻ to both boost charge separation and interact with H₂O₂/O₂ to produce ROS. In vivo experiments demonstrated the efficacy of this treatment without altering healthy tissues (Figure 11b).

At the interface between metal nanostructures and another media exists a delocalized coherent electron oscillation known as localized surface plasmon resonance (LSPR) [123]. Excitation of these electrons with a suitable wavelength excite them and favors their migration to the CB of the semiconductor, a phenomenon known as "hot-electron injection" [124] (Figure 12c). Li et al. fabricated MoSe₂-Au heterostructures with the capability of injecting hot-electrons from Au in the MoSe₂ CB under 808 nm irradiation [118]. Apart from enhancing the photocatalytic activity of MoSe₂ due hot electron process, Au is a typical catalyst to assist glucose oxidation [125,126]. Removing glucose from tumors interfere in their energy metabolism and has been proved an alternative therapeutic approach [127]. MoSe₂-Au photocatalyst effectively produce ROS under NIR irradiation while catalyzes glucose oxidation. This photoactivity exhibited an effective in vivo tumor inhibition (Figure 12d).

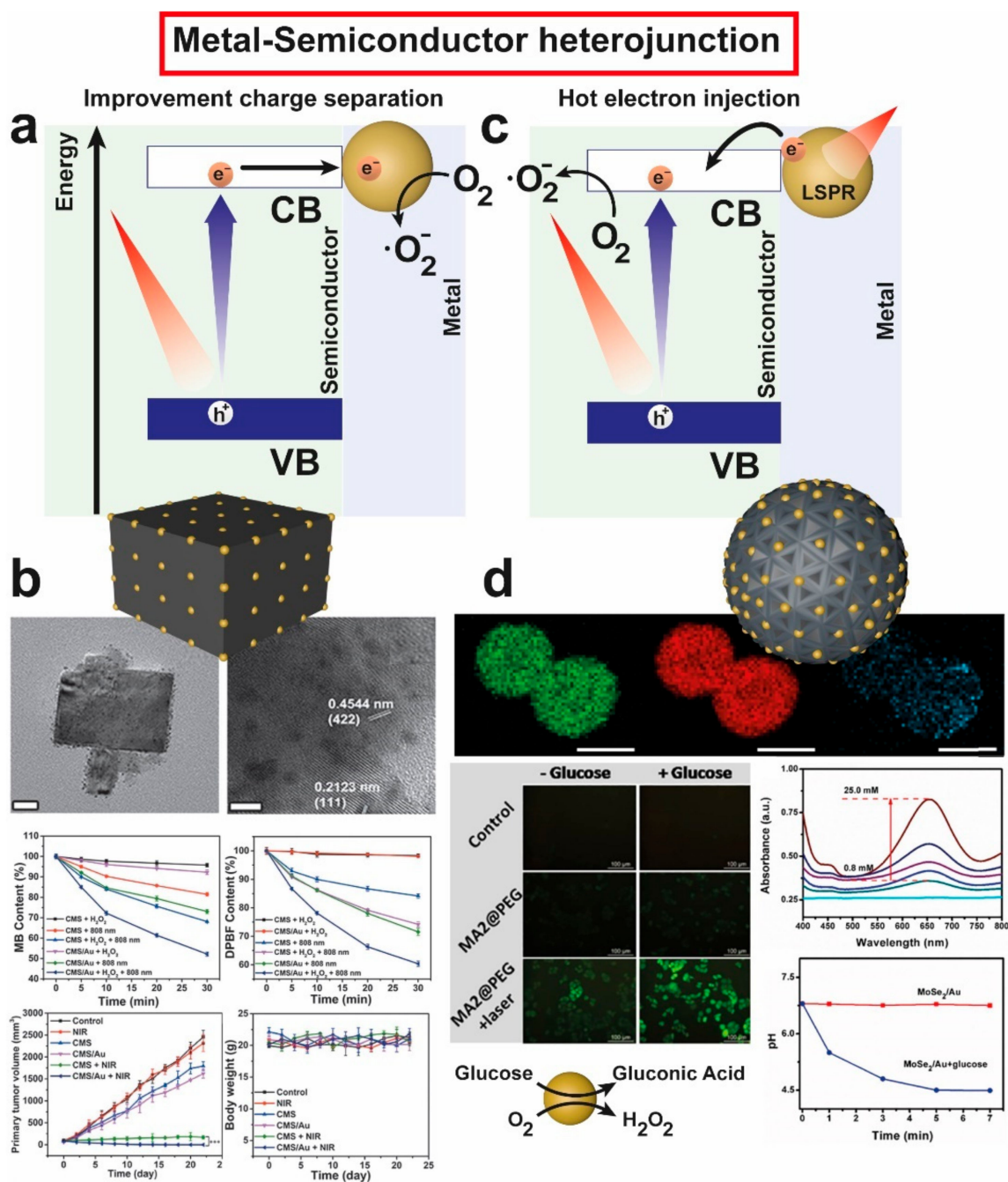


Figure 12. (a) Metal-semiconductor heterojunction band diagram. The presence of a noble-metal nanoparticle with a large work function (ϕ) since Au accepts photogenerated e^- to promote charge separation phenomena.; (b) TEM images of Cu₂MoS₄-Au heterostructure (left scale bar: 10 nm, right scale bar: 5 nm). Photogeneration of $\bullet\text{OH}$ and $\bullet\text{O}_2^-$ under NIR irradiation, enhanced by the introduction of Au nanoparticles in the nanostructure. Tumor inhibition of CuMoS₄-Au under 808 nm irradiation, without altering significantly mice body weight. Reprinted with permission from [116]. Copyright © 2020 WILEY-VCH Verlag GmbH & Co. KGaA, Weinheim; (c) Electron transference from the noble metal nanoparticle to CB of semiconductor through hot electron mechanism [123] (d) MoSe₂-Au nanoparticles elemental mapping (from left to right Mo, Se and Au) (scale bar: 200 nm). Glucose oxidase-like activity of Au nanoparticles on MoSe₂ surface, boosted by NIR irradiation for in vitro ROS generation. In vivo tumor inhibition by combining MoSe₂-Au with NIR irradiation. pH decreases in the presence of MoSe₂-Au catalyst, indicating the generation of gluconic acid as glucose oxidation product. Reprinted with permission from [118]. Copyright © 2021 Elsevier B.V.

5. Conclusions

The use of nanostructured photocatalysts in cancer therapy has paved the way to explore new and exciting therapeutic alternatives to treat cancer with the aid of visible and NIR irradiation light sources that can boost the in-situ generation of ROS in the tumor environment. Engineering smart nanomaterials towards synergistic heterostructure is key to overcome the drawbacks of organic photosensitizers applied in PDT or the limitations of single-phased materials. Likewise, exploring catalytic mechanisms that are well established in other catalytic fields (i.e., electrocatalysis) represents an appealing and exciting field when narrowed down to a cancer cell scenario. Classic reactions such as water splitting (i.e., H₂O transformation in O₂) or hydrogen evolution (H₂ generation from H⁺) are being now exploited to perform cancer therapy given favorable conditions in the TME. Finally, novel reactions in photocatalysis that directly target key metabolites (i.e., GSH, glucose) or favor biorthogonal processes are also of high interest in the field of cancer therapy and worth exploring in the forthcoming years.

Author Contributions: Conceptualization, J.B.-A. and J.L.H.; writing—original draft preparation, J.I.G.-P., J.B.-A. and J.L.H.; writing—review and editing, J.L.H. All authors have read and agreed to the published version of the manuscript.

Funding: This research was funded by the European Research Council (ERC) through an Advanced Research Grant (CADENCE, grant number 742684). The APC was waived by the journal.

Data Availability Statement: No new data were created or analyzed in this study. Data sharing is not applicable to this review.

Acknowledgments: The authors thank the Platform of Production of Biomaterials and Nanoparticles of the NANBIOSIS-ICTS of the CIBER in BioEngineering, Biomaterials & Nanomedicine (CIBER-BBN). J.B.-A. acknowledges the Spanish Government for a PhD predoctoral grant (FPU18/04618). J.I.G.-P. thanks the Regional Government of Aragon (DGA) for granting a PhD predoctoral contract. The Regional Government of Aragon is also acknowledged.

Conflicts of Interest: The authors declare no conflict of interest.

References

1. International Agency for Research Cancer (IARC)-WHO (Biennial Report 20–21). Available online: <https://www.iarc.who.int/biennial-report-2020-2021web/> (accessed on 24 January 2022).
2. Gai, S.; Yang, G.; Yang, P.; He, F.; Lin, J.; Jin, D.; Xing, B. Recent advances in functional nanomaterials for light-triggered cancer therapy. *Nano Today* **2018**, *19*, 146–187. [[CrossRef](#)]
3. Ash, C.; Dubec, M.; Donne, K.; Bashford, T. Effect of wavelength and beam width on penetration in light-tissue interaction using computational methods. *Lasers Med. Sci.* **2017**, *32*, 1909–1918. [[CrossRef](#)] [[PubMed](#)]
4. Alsaab, H.O.; Alghamdi, M.S.; Alotaibi, A.S.; Alzhrani, R.; Alwuthaynani, F.; Althobaiti, Y.S.; Almalki, A.H.; Sau, S.; Iyer, A.K. Progress in clinical trials of photodynamic therapy for solid tumors and the role of nanomedicine. *Cancers* **2020**, *12*, 2793. [[CrossRef](#)] [[PubMed](#)]
5. Phua, S.Z.F.; Xue, C.; Lim, W.Q.; Yang, G.; Chen, H.; Zhang, Y.; Wijaya, C.F.; Luo, Z.; Zhao, Y. Light-responsive prodrug-based supramolecular nanosystems for site-specific combination therapy of cancer. *Chem. Mater.* **2019**, *31*, 3349–3358. [[CrossRef](#)]
6. Wu, H.; Minamide, T.; Yano, T. Role of photodynamic therapy in the treatment of esophageal cancer. *Dig. Endosc. Off. J. Jpn. Gastroenterol. Endosc. Soc.* **2019**, *31*, 508–516. [[CrossRef](#)]
7. Anigo, E.C.; Plackal Adimuriyil George, B.; Abrahamse, H. The role of photodynamic therapy on multidrug resistant breast cancer. *Cancer Cell Int.* **2019**, *19*, 91. [[CrossRef](#)]
8. Nackiewicz, J.; Kliber-Jasik, M.; Skonieczna, M. A novel pro-apoptotic role of zinc octacarboxyphthalocyanine in melanoma me45 cancer cell's photodynamic therapy (PDT). *J. Photochem. Photobiol. B Biol.* **2019**, *190*, 146–153. [[CrossRef](#)]
9. Pellosi, D.S.; Tessaro, A.L.; Moret, F.; Gaio, E.; Reddi, E.; Caetano, W.; Quaglia, F.; Hioka, N. Pluronic[®] mixed micelles as efficient nanocarriers for benzoporphyrin derivatives applied to photodynamic therapy in cancer cells. *J. Photochem. Photobiol. A Chem.* **2016**, *314*, 143–154. [[CrossRef](#)]
10. Li, X.; Lee, S.; Yoon, J. Supramolecular photosensitizers rejuvenate photodynamic therapy. *Chem. Soc. Rev.* **2018**, *47*, 1174–1188. [[CrossRef](#)]
11. Yan, Y.; Zhang, J.; Ren, L.; Tang, C. Metal-containing and related polymers for biomedical applications. *Chem. Soc. Rev.* **2016**, *45*, 5232–5263. [[CrossRef](#)]

12. Zhou, Z.; Song, J.; Nie, L.; Chen, X. Reactive oxygen species generating systems meeting challenges of photodynamic cancer therapy. *Chem. Soc. Rev.* **2016**, *45*, 6597–6626. [[CrossRef](#)] [[PubMed](#)]
13. Fang, J.; Nakamura, H.; Maeda, H. The EPR effect: Unique features of tumor blood vessels for drug delivery, factors involved, and limitations and augmentation of the effect. *Adv. Drug Deliv. Rev.* **2011**, *63*, 136–151. [[CrossRef](#)] [[PubMed](#)]
14. Wade, L.G. *Organic Chemistry*; Pearson: London, UK, 2013.
15. Romero, N.A.; Nicewicz, D.A. Organic photoredox catalysis. *Chem. Rev.* **2016**, *116*, 10075–10166. [[CrossRef](#)]
16. Ohtani, B. Chapter 10-Photocatalysis by inorganic solid materials: Revisiting its definition, concepts, and experimental procedures. In *Advances in Inorganic Chemistry*; van Eldik, R., Stochel, G., Eds.; Academic Press: Cambridge, MA, USA, 2011; Volume 63, pp. 395–430.
17. Tian, J.; Hao, P.; Wei, N.; Cui, H.; Liu, H. 3D Bi₂MoO₆ nanosheet/TiO₂ nanobelt heterostructure: Enhanced photocatalytic activities and photoelectrochemistry performance. *ACS Catal.* **2015**, *5*, 4530–4536. [[CrossRef](#)]
18. Fu, J.; Yu, J.; Jiang, C.; Cheng, B. g-C₃N₄-based heterostructured photocatalysts. *Adv. Energy Mater.* **2018**, *8*, 1701503. [[CrossRef](#)]
19. Yuan, Y.-P.; Ruan, L.-W.; Barber, J.; Joachim Loo, S.C.; Xue, C. Hetero-nanostructured suspended photocatalysts for solar-to-fuel conversion. *Energy Environ. Sci.* **2014**, *7*, 3934–3951. [[CrossRef](#)]
20. Krumova, K.; Cosa, G. Chapter 1 Overview of Reactive Oxygen Species. In *Singlet Oxygen: Applications in Biosciences and Nanosciences, Volume 1*; The Royal Society of Chemistry: London, UK, 2016; Volume 1, pp. 1–21.
21. Chen, W.; Sun, Z.; Jiang, C.; Sun, W.; Yu, B.; Wang, W.; Lu, L. An all-in-one organic semiconductor for targeted photooxidation catalysis in hypoxic tumor. *Angew. Chem. Int. Ed.* **2021**, *60*, 16641–16648. [[CrossRef](#)]
22. Ding, Y.; Dai, Y.; Wu, M.; Li, L. Glutathione-mediated nanomedicines for cancer diagnosis and therapy. *Chem. Eng. J.* **2021**, *426*, 128880. [[CrossRef](#)]
23. Zhao, B.; Wang, Y.; Yao, X.; Chen, D.; Fan, M.; Jin, Z.; He, Q. Photocatalysis-mediated drug-free sustainable cancer therapy using nanocatalyst. *Nat. Commun.* **2021**, *12*, 1345. [[CrossRef](#)]
24. Höckel, M.; Vaupel, P. Tumor hypoxia: Definitions and current clinical, biologic, and molecular aspects. *JNCI J. Natl. Cancer Inst.* **2001**, *93*, 266–276. [[CrossRef](#)]
25. Ruan, C.; Su, K.; Zhao, D.; Lu, A.; Zhong, C. Nanomaterials for tumor hypoxia relief to improve the efficacy of ROS-generated cancer therapy. *Front. Chem.* **2021**, *9*, 649158. [[CrossRef](#)] [[PubMed](#)]
26. Nelson, D.L.; Lehninger, A.L.; Cox, M.M. *Lehninger Principles of Biochemistry*; W.H. Freeman: New York, NY, USA, 2008.
27. Balendiran, G.K.; Dabur, R.; Fraser, D. The role of glutathione in cancer. *Cell Biochem. Funct.* **2004**, *22*, 343–352. [[CrossRef](#)] [[PubMed](#)]
28. Dykman, L.; Khlebtsov, N. Gold nanoparticles in biomedical applications: Recent advances and perspectives. *Chem. Soc. Rev.* **2012**, *41*, 2256–2282. [[CrossRef](#)]
29. Guo, J.; Rahme, K.; He, Y.; Li, L.L.; Holmes, J.D.; O'Driscoll, C.M. Gold nanoparticles enlighten the future of cancer theranostics. *Int. J. Nanomed.* **2017**, *12*, 6131–6152. [[CrossRef](#)] [[PubMed](#)]
30. Pedone, D.; Moglianetti, M.; De Luca, E.; Bardi, G.; Pompa, P.P. Platinum nanoparticles in nanobiomedicine. *Chem. Soc. Rev.* **2017**, *46*, 4951–4975. [[CrossRef](#)]
31. Ma, N.; Wu, F.-G.; Zhang, X.; Jiang, Y.-W.; Jia, H.-R.; Wang, H.-Y.; Li, Y.-H.; Liu, P.; Gu, N.; Chen, Z. Shape-dependent radiosensitization effect of gold nanostructures in cancer radiotherapy: Comparison of gold nanoparticles, nanopikes, and nanorods. *ACS Appl. Mater. Interfaces* **2017**, *9*, 13037–13048. [[CrossRef](#)]
32. Cao, Y.; Wu, T.; Dai, W.; Dong, H.; Zhang, X. TiO₂ nanosheets with the Au nanocrystal-decorated edge for mitochondria-targeting enhanced sonodynamic therapy. *Chem. Mater.* **2019**, *31*, 9105–9114. [[CrossRef](#)]
33. Gu, T.; Wang, Y.; Lu, Y.; Cheng, L.; Feng, L.; Zhang, H.; Li, X.; Han, G.; Liu, Z. Platinum nanoparticles to enable electrodynamic therapy for effective cancer treatment. *Adv. Mater.* **2019**, *31*, 1806803. [[CrossRef](#)]
34. Li, J.; Liu, W.; Wu, X.; Gao, X. Mechanism of pH-switchable peroxidase and catalase-like activities of gold, silver, platinum and palladium. *Biomaterials* **2015**, *48*, 37–44. [[CrossRef](#)]
35. Chen, Q.; He, S.; Zhang, F.; Cui, F.; Liu, J.; Wang, M.; Wang, D.; Jin, Z.; Li, C. A versatile Pt-Ce₆ nanoplatform as catalase nanozyme and NIR-II photothermal agent for enhanced PDT/PTT tumor therapy. *Sci. China Mater.* **2021**, *64*, 510–530. [[CrossRef](#)]
36. Alkilany, A.M.; Thompson, L.B.; Boulos, S.P.; Sisco, P.N.; Murphy, C.J. Gold nanorods: Their potential for photothermal therapeutics and drug delivery, tempered by the complexity of their biological interactions. *Adv. Drug Deliv. Rev.* **2012**, *64*, 190–199. [[CrossRef](#)] [[PubMed](#)]
37. He, J.-S.; Liu, S.-J.; Zhang, Y.-R.; Chu, X.-D.; Lin, Z.-B.; Zhao, Z.; Qiu, S.-H.; Guo, Y.-G.; Ding, H.; Pan, Y.-L.; et al. The application of and strategy for gold nanoparticles in cancer immunotherapy. *Front. Pharmacol.* **2021**, *12*, 1430. [[CrossRef](#)] [[PubMed](#)]
38. Ming, J.; Zhu, T.; Yang, W.; Shi, Y.; Huang, D.; Li, J.; Xiang, S.; Wang, J.; Chen, X.; Zheng, N. Pd@Pt-GOx/HA as a novel enzymatic cascade nanoreactor for high-efficiency starving-enhanced chemodynamic cancer therapy. *ACS Appl. Mater. Interfaces* **2020**, *12*, 51249–51262. [[CrossRef](#)] [[PubMed](#)]
39. Sancho-Alberro, M.; Rubio-Ruiz, B.; Pérez-López, A.M.; Sebastián, V.; Martín-Duque, P.; Arruebo, M.; Santamaría, J.; Unciti-Broceta, A. Cancer-derived exosomes loaded with ultrathin palladium nanosheets for targeted bioorthogonal catalysis. *Nat. Catal.* **2019**, *2*, 864–872. [[CrossRef](#)] [[PubMed](#)]

40. Pérez-López, A.M.; Rubio-Ruiz, B.; Valero, T.; Contreras-Montoya, R.; Álvarez de Cienfuegos, L.; Sebastián, V.; Santamaría, J.; Unciti-Broceta, A. Bioorthogonal uncaging of cytotoxic paclitaxel through Pd nanosheet–hydrogel frameworks. *J. Med. Chem.* **2020**, *63*, 9650–9659. [[CrossRef](#)]
41. Ali, M.R.K.; Wu, Y.; El-Sayed, M.A. Gold-nanoparticle-assisted plasmonic photothermal therapy advances toward clinical application. *J. Phys. Chem. C* **2019**, *123*, 15375–15393. [[CrossRef](#)]
42. Lv, Z.; He, S.; Wang, Y.; Zhu, X. Noble metal nanomaterials for nir-triggered photothermal therapy in cancer. *Adv. Heal. Mater.* **2021**, *10*, 2001806. [[CrossRef](#)]
43. Vankayala, R.; Sagadevan, A.; Vijayaraghavan, P.; Kuo, C.-L.; Hwang, K.C. Metal nanoparticles sensitize the formation of singlet oxygen. *Angew. Chem. Int. Ed.* **2011**, *50*, 10640–10644. [[CrossRef](#)]
44. Shinde, D.R.; Tambade, P.S.; Chaskar, M.G.; Gadave, K.M. Photocatalytic degradation of dyes in water by analytical reagent grades ZnO, TiO₂ and SnO₂: A comparative study. *Drink. Water Eng. Sci.* **2017**, *10*, 109–117. [[CrossRef](#)]
45. Upadhyay, G.K.; Rajput, J.K.; Pathak, T.K.; Kumar, V.; Purohit, L.P. Synthesis of ZnO: TiO₂ nanocomposites for photocatalyst application in visible light. *Vacuum* **2019**, *160*, 154–163. [[CrossRef](#)]
46. Kippeny, T.; Swafford, L.A.; Rosenthal, S.J. Semiconductor nanocrystals: A powerful visual aid for introducing the particle in a box. *J. Chem. Educ.* **2002**, *79*, 1094. [[CrossRef](#)]
47. Wang, H.; Yang, X.; Shao, W.; Chen, S.; Xie, J.; Zhang, X.; Wang, J.; Xie, Y. Ultrathin black phosphorus nanosheets for efficient singlet oxygen generation. *J. Am. Chem. Soc.* **2015**, *137*, 11376–11382. [[CrossRef](#)] [[PubMed](#)]
48. Dong, H.; Tang, S.; Hao, Y.; Yu, H.; Dai, W.; Zhao, G.; Cao, Y.; Lu, H.; Zhang, X.; Ju, H. Fluorescent MoS₂ quantum dots: Ultrasonic preparation, up-conversion and down-conversion bioimaging, and photodynamic therapy. *ACS Appl. Mater. Interfaces* **2016**, *8*, 3107–3114. [[CrossRef](#)] [[PubMed](#)]
49. Guo, W.; Guo, C.; Zheng, N.; Sun, T.; Liu, S. CsxWO₃ nanorods coated with polyelectrolyte multilayers as a multifunctional nanomaterial for bimodal imaging-guided photothermal/photodynamic cancer treatment. *Adv. Mater.* **2017**, *29*, 1604157. [[CrossRef](#)]
50. Li, Y.; Liu, Z.; Hou, Y.; Yang, G.; Fei, X.; Zhao, H.; Guo, Y.; Su, C.; Wang, Z.; Zhong, H.; et al. Multifunctional nanoplatfrom based on black phosphorus quantum dots for bioimaging and photodynamic/photothermal synergistic cancer therapy. *ACS Appl. Mater. Interfaces* **2017**, *9*, 25098–25106. [[CrossRef](#)]
51. Xu, Y.; Fan, M.; Yang, W.; Xiao, Y.; Zeng, L.; Wu, X.; Xu, Q.; Su, C.; He, Q. Homogeneous carbon/potassium-incorporation strategy for synthesizing red polymeric carbon nitride capable of near-infrared photocatalytic H₂ production. *Adv. Mater.* **2021**, *33*, 2101455. [[CrossRef](#)]
52. Duo, Y.; Luo, G.; Li, Z.; Chen, Z.; Li, X.; Jiang, Z.; Yu, B.; Huang, H.; Sun, Z.; Yu, X.-F. Photothermal and enhanced photocatalytic therapies conduce to synergistic anticancer phototherapy with biodegradable titanium diselenide nanosheets. *Small* **2021**, *17*, 2103239. [[CrossRef](#)]
53. Mou, J.; Lin, T.; Huang, F.; Chen, H.; Shi, J. Black titania-based theranostic nanoplatfrom for single NIR laser induced dual-modal imaging-guided PTT/PDT. *Biomaterials* **2016**, *84*, 13–24. [[CrossRef](#)]
54. Mou, J.; Lin, T.; Huang, F.; Shi, J.; Chen, H. A new green titania with enhanced nir absorption for mitochondria-targeted cancer therapy. *Theranostics* **2017**, *7*, 1531–1542. [[CrossRef](#)]
55. Yu, H.; Cheng, Y.; Wen, C.; Sun, Y.-Q.; Yin, X.-B. Triple cascade nanocatalyst with laser-activatable O₂ supply and photothermal enhancement for effective catalytic therapy against hypoxic tumor. *Biomaterials* **2022**, *280*, 121308. [[CrossRef](#)]
56. Murakami, T.; Nakatsuji, H.; Inada, M.; Matoba, Y.; Umeyama, T.; Tsujimoto, M.; Isoda, S.; Hashida, M.; Imahori, H. Photodynamic and photothermal effects of semiconducting and metallic-enriched single-walled carbon nanotubes. *J. Am. Chem. Soc.* **2012**, *134*, 17862–17865. [[CrossRef](#)] [[PubMed](#)]
57. Kalluru, P.; Vankayala, R.; Chiang, C.-S.; Hwang, K.C. Nano-graphene oxide-mediated In vivo fluorescence imaging and bimodal photodynamic and photothermal destruction of tumors. *Biomaterials* **2016**, *95*, 1–10. [[CrossRef](#)] [[PubMed](#)]
58. Shi, J.; Wang, L.; Gao, J.; Liu, Y.; Zhang, J.; Ma, R.; Liu, R.; Zhang, Z. A fullerene-based multi-functional nanoplatfrom for cancer theranostic applications. *Biomaterials* **2014**, *35*, 5771–5784. [[CrossRef](#)] [[PubMed](#)]
59. Ortega-Liebana, M.C.; Encabo-Berzosa, M.M.; Casanova, A.; Pereboom, M.D.; Alda, J.O.; Hueso, J.L.; Santamaria, J. Upconverting carbon nanodots from Ethylenediaminetetraacetic Acid (EDTA) as near-infrared activated phototheranostic agents. *Chem.-A Eur. J.* **2019**, *25*, 5539–5546. [[CrossRef](#)] [[PubMed](#)]
60. Li, Y.; Zheng, X.; Zhang, X.; Liu, S.; Pei, Q.; Zheng, M.; Xie, Z. Porphyrin-based carbon dots for photodynamic therapy of hepatoma. *Adv. Healthc. Mater.* **2017**, *6*, 1600924. [[CrossRef](#)]
61. Zhang, K.; Meng, X.; Cao, Y.; Yang, Z.; Dong, H.; Zhang, Y.; Lu, H.; Shi, Z.; Zhang, X. Metal–Organic framework nanoshuttle for synergistic photodynamic and low-temperature photothermal therapy. *Adv. Funct. Mater.* **2018**, *28*, 1804634. [[CrossRef](#)]
62. Zheng, X.; Wang, L.; Liu, M.; Lei, P.; Liu, F.; Xie, Z. Nanoscale mixed-component metal–organic frameworks with photosensitizer spatial-arrangement-dependent photochemistry for multimodal-imaging-guided photothermal therapy. *Chem. Mater.* **2018**, *30*, 6867–6876. [[CrossRef](#)]
63. Li, S.-H.; Yang, W.; Liu, Y.; Song, X.-R.; Liu, R.; Chen, G.; Lu, C.-H.; Yang, H.-H. Engineering of tungsten carbide nanoparticles for imaging-guided single 1064 nm laser-activated dual-type photodynamic and photothermal therapy of cancer. *Nano Res.* **2018**, *11*, 4859–4873. [[CrossRef](#)]

64. Hou, H.; Wang, Z.; Ma, Y.; Yu, K.; Zhao, J.; Lin, H.; Qu, F. NIR-driven intracellular photocatalytic oxygen-supply on metallic molybdenum carbide@N-carbon for hypoxic tumor therapy. *J. Colloid Interface Sci.* **2022**, *607*, 1–15. [[CrossRef](#)]
65. Lv, R.; Yang, D.; Yang, P.; Xu, J.; He, F.; Gai, S.; Li, C.; Dai, Y.; Yang, G.; Lin, J. Integration of upconversion nanoparticles and ultrathin black phosphorus for efficient photodynamic theranostics under 808 nm near-infrared light irradiation. *Chem. Mater.* **2016**, *28*, 4724–4734. [[CrossRef](#)]
66. Tran, V.; Soklaski, R.; Liang, Y.; Yang, L. Layer-controlled band gap and anisotropic excitons in few-layer black phosphorus. *Phys. Rev. B* **2014**, *89*, 235319. [[CrossRef](#)]
67. Wang, Y.L.; Nie, T.; Li, Y.H.; Wang, X.L.; Zheng, L.R.; Chen, A.P.; Gong, X.Q.; Yang, H.G. Black tungsten nitride as a metallic photocatalyst for overall water splitting operable at up to 765 nm. *Angew. Chem. (Int. Ed. Engl.)* **2017**, *56*, 7430–7434. [[CrossRef](#)] [[PubMed](#)]
68. Nocito, G.; Calabrese, G.; Forte, S.; Petralia, S.; Puglisi, C.; Campolo, M.; Esposito, E.; Conoci, S. Carbon dots as promising tools for cancer diagnosis and therapy. *Cancers* **2021**, *13*, 1991. [[CrossRef](#)]
69. Wang, J.; Xu, M.; Wang, D.; Li, Z.; Primo, F.L.; Tedesco, A.C.; Bi, H. Copper-doped carbon dots for optical bioimaging and photodynamic therapy. *Inorg. Chem.* **2019**, *58*, 13394–13402. [[CrossRef](#)]
70. Chen, G.; Qiu, H.; Prasad, P.N.; Chen, X. Upconversion nanoparticles: Design, nanochemistry, and applications in theranostics. *Chem. Rev.* **2014**, *114*, 5161–5214. [[CrossRef](#)] [[PubMed](#)]
71. Wang, L.; Wang, K.; He, T.; Zhao, Y.; Song, H.; Wang, H. Graphitic carbon nitride-based photocatalytic materials: Preparation strategy and application. *ACS Sustain. Chem. Eng.* **2020**, *8*, 16048–16085. [[CrossRef](#)]
72. Chan, M.-H.; Chen, C.-W.; Lee, I.J.; Chan, Y.-C.; Tu, D.; Hsiao, M.; Chen, C.-H.; Chen, X.; Liu, R.-S. Near-infrared light-mediated photodynamic therapy nanoplatfrom by the electrostatic assembly of upconversion nanoparticles with graphitic carbon nitride quantum dots. *Inorg. Chem.* **2016**, *55*, 10267–10277. [[CrossRef](#)] [[PubMed](#)]
73. Chan, M.-H.; Pan, Y.-T.; Lee, I.-J.; Chen, C.-W.; Chan, Y.-C.; Hsiao, M.; Wang, F.; Sun, L.; Chen, X.; Liu, R.-S. Minimizing the heat effect of photodynamic therapy based on inorganic nanocomposites mediated by 808 nm near-infrared light. *Small* **2017**, *13*, 1700038. [[CrossRef](#)]
74. Feng, L.; He, F.; Yang, G.; Gai, S.; Dai, Y.; Li, C.; Yang, P. NIR-driven graphitic-phase carbon nitride nanosheets for efficient bioimaging and photodynamic therapy. *J. Mater. Chem. B* **2016**, *4*, 8000–8008. [[CrossRef](#)]
75. Brown, J.M. Tumor hypoxia in cancer therapy. *Methods Enzymol.* **2007**, *435*, 297–321. [[CrossRef](#)]
76. Tetsuka, H.; Asahi, R.; Nagoya, A.; Okamoto, K.; Tajima, I.; Ohta, R.; Okamoto, A. Optically tunable amino-functionalized graphene quantum dots. *Adv. Mater.* **2012**, *24*, 5333–5338. [[CrossRef](#)] [[PubMed](#)]
77. Zeng, J.-Y.; Zhang, M.-K.; Peng, M.-Y.; Gong, D.; Zhang, X.-Z. Porphyrinic metal–organic frameworks coated gold nanorods as a versatile nanoplatfrom for combined photodynamic/photothermal/chemotherapy of tumor. *Adv. Funct. Mater.* **2018**, *28*, 1705451. [[CrossRef](#)]
78. Wei, J.; Li, J.; Sun, D.; Li, Q.; Ma, J.; Chen, X.; Zhu, X.; Zheng, N. A novel theranostic nanoplatfrom based on Pd@Pt-PEG-Ce6 for enhanced photodynamic therapy by modulating tumor hypoxia microenvironment. *Adv. Funct. Mater.* **2018**, *28*, 1706310. [[CrossRef](#)]
79. Wang, M.; Chang, M.; Chen, Q.; Wang, D.; Li, C.; Hou, Z.; Lin, J.; Jin, D.; Xing, B. Au2Pt-PEG-Ce6 nanoformulation with dual nanozyme activities for synergistic chemodynamic therapy/phototherapy. *Biomaterials* **2020**, *252*, 120093. [[CrossRef](#)]
80. Yan, J.; Sun, H.; Li, J.; Qi, W.; Wang, H. A theranostic plaster combining photothermal therapy and photodynamic therapy based on chlorin e6/gold nanorods (Ce6/Au nrs) composite. *Colloids Surf. A Physicochem. Eng. Asp.* **2018**, *537*, 460–466. [[CrossRef](#)]
81. Kotiaho, A.; Lahtinen, R.; Efimov, A.; Metsberg, H.-K.; Sariola, E.; Lehtivuori, H.; Tkachenko, N.V.; Lemmetyinen, H. Photoinduced charge and energy transfer in phthalocyanine-functionalized gold nanoparticles. *J. Phys. Chem. C* **2010**, *114*, 162–168. [[CrossRef](#)]
82. Vankayala, R.; Kuo, C.-L.; Sagadevan, A.; Chen, P.-H.; Chiang, C.-S.; Hwang, K.C. Morphology dependent photosensitization and formation of singlet oxygen ($^1\Delta_g$) by gold and silver nanoparticles and its application in cancer treatment. *J. Mater. Chem. B* **2013**, *1*, 4379–4387. [[CrossRef](#)]
83. Pasparakis, G. Light-induced generation of singlet oxygen by naked gold nanoparticles and its implications to cancer cell phototherapy. *Small* **2013**, *9*, 4130–4134. [[CrossRef](#)]
84. Chadwick, S.J.; Salah, D.; Livesey, P.M.; Brust, M.; Volk, M. Singlet oxygen generation by laser irradiation of gold nanoparticles. *J. Phys. Chem. C* **2016**, *120*, 10647–10657. [[CrossRef](#)]
85. Zhao, T.; Shen, X.; Li, L.; Guan, Z.; Gao, N.; Yuan, P.; Yao, S.Q.; Xu, Q.-H.; Xu, G.Q. Gold nanorods as dual photo-sensitizing and imaging agents for two-photon photodynamic therapy. *Nanoscale* **2012**, *4*, 7712–7719. [[CrossRef](#)]
86. Jiang, C.; Zhao, T.; Yuan, P.; Gao, N.; Pan, Y.; Guan, Z.; Zhou, N.; Xu, Q.-H. Two-photon induced photoluminescence and singlet oxygen generation from aggregated gold nanoparticles. *ACS Appl. Mater. Interfaces* **2013**, *5*, 4972–4977. [[CrossRef](#)] [[PubMed](#)]
87. Lazarides, A.A.; Lance Kelly, K.; Jensen, T.R.; Schatz, G.C. Optical properties of metal nanoparticles and nanoparticle aggregates important in biosensors. *J. Mol. Struct. THEOCHEM* **2000**, *529*, 59–63. [[CrossRef](#)]
88. Albanese, A.; Chan, W.C.W. Effect of gold nanoparticle aggregation on cell uptake and toxicity. *ACS Nano* **2011**, *5*, 5478–5489. [[CrossRef](#)] [[PubMed](#)]
89. Yang, Y.; Hu, Y.; Du, H.; Wang, H. Intracellular gold nanoparticle aggregation and their potential applications in photodynamic therapy. *Chem. Commun.* **2014**, *50*, 7287–7290. [[CrossRef](#)]

90. Vankayala, R.; Huang, Y.-K.; Kalluru, P.; Chiang, C.-S.; Hwang, K.C. First demonstration of gold nanorods-mediated photodynamic therapeutic destruction of tumors via near infra-red light activation. *Small* **2014**, *10*, 1612–1622. [[CrossRef](#)]
91. Vijayaraghavan, P.; Liu, C.-H.; Vankayala, R.; Chiang, C.-S.; Hwang, K.C. Designing multi-branched gold nanoechinus for nir light activated dual modal photodynamic and photothermal therapy in the second biological window. *Adv. Mater.* **2014**, *26*, 6689–6695. [[CrossRef](#)]
92. Boyer, J.-C.; van Veggel, F.C.J.M. Absolute quantum yield measurements of colloidal NaYF₄: Er³⁺, Yb³⁺ upconverting nanoparticles. *Nanoscale* **2010**, *2*, 1417–1419. [[CrossRef](#)]
93. Li, S.; Gu, K.; Wang, H.; Xu, B.; Li, H.; Shi, X.; Huang, Z.; Liu, H. Degradable holey palladium nanosheets with highly active 1d nanoholes for synergetic phototherapy of hypoxic tumors. *J. Am. Chem. Soc.* **2020**, *142*, 5649–5656. [[CrossRef](#)]
94. Vankayala, R.; Kuo, C.-L.; Nuthalapati, K.; Chiang, C.-S.; Hwang, K.C. Nucleus-targeting gold nanoclusters for simultaneous in vivo fluorescence imaging, gene delivery, and nir-light activated photodynamic therapy. *Adv. Funct. Mater.* **2015**, *25*, 5934–5945. [[CrossRef](#)]
95. Chen, Q.; Chen, J.; Yang, Z.; Zhang, L.; Dong, Z.; Liu, Z. NIR-II light activated photodynamic therapy with protein-capped gold nanoclusters. *Nano Res.* **2018**, *11*, 5657–5669. [[CrossRef](#)]
96. Yu, Y.; Geng, J.; Ong, E.Y.X.; Chellappan, V.; Tan, Y.N. Bovine serum albumin protein-templated silver nanocluster (BSA-Ag₁₃): An effective singlet oxygen generator for photodynamic cancer therapy. *Adv. Heal. Mater.* **2016**, *5*, 2528–2535. [[CrossRef](#)] [[PubMed](#)]
97. Yang, Y.; Chen, M.; Wang, B.; Wang, P.; Liu, Y.; Zhao, Y.; Li, K.; Song, G.; Zhang, X.-B.; Tan, W. NIR-II driven plasmon-enhanced catalysis for a timely supply of oxygen to overcome hypoxia-induced radiotherapy tolerance. *Angew. Chem. Int. Ed.* **2019**, *58*, 15069–15075. [[CrossRef](#)] [[PubMed](#)]
98. Liu, X.; Wan, Y.; Jiang, T.; Zhang, Y.; Huang, P.; Tang, L. Plasmon-activated nanozymes with enhanced catalytic activity by near-infrared light irradiation. *Chem. Commun.* **2020**, *56*, 1784–1787. [[CrossRef](#)] [[PubMed](#)]
99. Liu, P.; Yang, W.; Shi, L.; Zhang, H.; Xu, Y.; Wang, P.; Zhang, G.; Chen, W.R.; Zhang, B.; Wang, X. Concurrent photothermal therapy and photodynamic therapy for cutaneous squamous cell carcinoma by gold nanoclusters under a single NIR laser irradiation. *J. Mater. Chem. B* **2019**, *7*, 6924–6933. [[CrossRef](#)]
100. Sakamoto, M.; Tachikawa, T.; Fujitsuka, M.; Majima, T. Photochemical reactivity of gold clusters: Dependence on size and spin multiplicity. *Langmuir* **2009**, *25*, 13888–13893. [[CrossRef](#)]
101. Das, T.; Ghosh, P.; Shanavas, M.S.; Maity, A.; Mondal, S.; Purkayastha, P. Protein-templated gold nanoclusters: Size dependent inversion of fluorescence emission in the presence of molecular oxygen. *Nanoscale* **2012**, *4*, 6018–6024. [[CrossRef](#)]
102. Cui, M.; Zhao, Y.; Song, Q. Synthesis, optical properties and applications of ultra-small luminescent gold nanoclusters. *Trends Anal. Chem.* **2014**, *57*, 73–82. [[CrossRef](#)]
103. Lillo, C.R.; Calienni, M.N.; Rivas Aiello, B.; Prieto, M.J.; Rodriguez Sartori, D.; Tuninetti, J.; Toledo, P.; Alonso, S.D.V.; Moya, S.; Gonzalez, M.C.; et al. BSA-capped gold nanoclusters as potential theragnostic for skin diseases: Photoactivation, skin penetration, in vitro, and in vivo toxicity. *Mater. Sci. Eng. C* **2020**, *112*, 110891. [[CrossRef](#)]
104. Poderys, V.; Jarockyte, G.; Bagdonas, S.; Karabanovas, V.; Rotomskis, R. Protein-stabilized gold nanoclusters for PDT: ROS and singlet oxygen generation. *J. Photochem. Photobiol. B Biol.* **2020**, *204*, 111802. [[CrossRef](#)]
105. Sies, H.; Menck, C.F.M. Singlet oxygen induced DNA damage. *Mutat. Res./DNAging* **1992**, *275*, 367–375. [[CrossRef](#)]
106. Ravanat, J.-L.; Di Mascio, P.; Martinez, G.R.; Medeiros, M.H.G.; Cadet, J. Singlet oxygen induces oxidation of cellular DNA*. *J. Biol. Chem.* **2000**, *275*, 40601–40604. [[CrossRef](#)] [[PubMed](#)]
107. Chen, Q.; Chen, J.; Liang, C.; Feng, L.; Dong, Z.; Song, X.; Song, G.; Liu, Z. Drug-induced co-assembly of albumin/catalase as smart nano-theranostics for deep intra-tumoral penetration, hypoxia relieve, and synergistic combination therapy. *J. Control. Release Off. J. Control. Release Soc.* **2017**, *263*, 79–89. [[CrossRef](#)]
108. Kong, N.; Zhang, H.; Feng, C.; Liu, C.; Xiao, Y.; Zhang, X.; Mei, L.; Kim, J.S.; Tao, W.; Ji, X. Arsenene-mediated multiple independently targeted reactive oxygen species burst for cancer therapy. *Nat. Commun.* **2021**, *12*, 4777. [[CrossRef](#)] [[PubMed](#)]
109. Zhen, W.; Liu, Y.; Jia, X.; Wu, L.; Wang, C.; Jiang, X. Reductive surfactant-assisted one-step fabrication of a BiOI/BiOI₃ heterojunction biophotocatalyst for enhanced photodynamic theranostics overcoming tumor hypoxia. *Nanoscale Horiz.* **2019**, *4*, 720–726. [[CrossRef](#)]
110. Guo, Z.; Zhu, S.; Yong, Y.; Zhang, X.; Dong, X.; Du, J.; Xie, J.; Wang, Q.; Gu, Z.; Zhao, Y. Synthesis of BSA-coated BiOI@Bi₂S₃ semiconductor heterojunction nanoparticles and their applications for radio/photodynamic/photothermal synergistic therapy of tumor. *Adv. Mater.* **2017**, *29*, 1704136. [[CrossRef](#)] [[PubMed](#)]
111. Kang, Y.; Li, Z.; Yang, Y.; Su, Z.; Ji, X.; Zhang, S. Antimonene nanosheets-based z-scheme heterostructure with enhanced reactive oxygen species generation and photothermal conversion efficiency for photonic therapy of cancer. *Adv. Healthc. Mater.* **2021**, *10*, 2001835. [[CrossRef](#)]
112. Pan, C.; Ou, M.; Cheng, Q.; Zhou, Y.; Yu, Y.; Li, Z.; Zhang, F.; Xia, D.; Mei, L.; Ji, X. Z-scheme Heterojunction functionalized pyrite Nanosheets for modulating tumor microenvironment and strengthening photo/Chemodynamic therapeutic effects. *Adv. Funct. Mater.* **2020**, *30*, 1906466. [[CrossRef](#)]
113. Cheng, Y.; Kong, X.; Chang, Y.; Feng, Y.; Zheng, R.; Wu, X.; Xu, K.; Gao, X.; Zhang, H. Spatiotemporally synchronous oxygen self-supply and reactive oxygen species production on z-scheme heterostructures for hypoxic tumor therapy. *Adv. Mater.* **2020**, *32*, 1908109. [[CrossRef](#)]

114. Wang, Q.; Ji, Y.; Shi, J.; Wang, L. NIR-driven water splitting H₂ production nanoplatfor for H₂-mediated cascade-amplifying synergetic cancer therapy. *ACS Appl. Mater. Interfaces* **2020**, *12*, 23677–23688. [[CrossRef](#)]
115. Sang, D.; Wang, K.; Sun, X.; Wang, Y.; Lin, H.; Jia, R.; Qu, F. NIR-driven intracellular photocatalytic O₂ evolution on Z-scheme Ni₃S₂/Cu_{1.8}S@HA for hypoxic tumor therapy. *ACS Appl. Mater. Interfaces* **2021**, *13*, 9604–9619. [[CrossRef](#)]
116. Chang, M.; Hou, Z.; Wang, M.; Wang, M.; Dang, P.; Liu, J.; Shu, M.; Ding, B.; Al Kheraif, A.A.; Li, C.; et al. Cu₂MoS₄/Au heterostructures with enhanced catalase-like activity and photoconversion efficiency for primary/metastatic tumors eradication by phototherapy-induced immunotherapy. *Small* **2020**, *16*, 1907146. [[CrossRef](#)] [[PubMed](#)]
117. Yang, D.; Gulzar, A.; Yang, G.; Gai, S.; He, F.; Dai, Y.; Zhong, C.; Yang, P. Au nanoclusters sensitized black TiO₂-x nanotubes for enhanced photodynamic therapy driven by near-infrared light. *Small* **2017**, *13*, 1703007. [[CrossRef](#)] [[PubMed](#)]
118. Li, Y.; Wang, L.; Kang, K.; Ma, Y.; Yu, K.; Lu, T.; Qu, F.; Lin, H. All in one theranostic nanoagent based on MoSe₂/Au@PEG hollow nanospheres for the enhanced synergetic antitumor. *Chem. Eng. J.* **2022**, *429*, 132330. [[CrossRef](#)]
119. Zhang, Z.; Huang, J.; Fang, Y.; Zhang, M.; Liu, K.; Dong, B. A nonmetal plasmonic Z-scheme photocatalyst with UV- to NIR-driven photocatalytic protons reduction. *Adv. Mater.* **2017**, *29*, 1606688. [[CrossRef](#)]
120. Xiao, L.; Liu, T.; Zhang, M.; Li, Q.; Yang, J. Interfacial construction of zero-dimensional/one-dimensional g-C₃N₄ nanoparticles/TiO₂ nanotube arrays with Z-scheme heterostructure for improved photoelectrochemical water splitting. *ACS Sustain. Chem. Eng.* **2019**, *7*, 2483–2491. [[CrossRef](#)]
121. Kou, Z.; Zhao, P.; Wang, Z.; Jin, Z.; Chen, L.; Su, B.-L.; He, Q. Acid-responsive H₂-releasing Fe nanoparticles for safe and effective cancer therapy. *J. Mater. Chem. B* **2019**, *7*, 2759–2765. [[CrossRef](#)] [[PubMed](#)]
122. Fan, M.; Wen, Y.; Ye, D.; Jin, Z.; Zhao, P.; Chen, D.; Lu, X.; He, Q. Acid-responsive H₂-releasing 2D MgB₂ nanosheet for therapeutic synergy and side effect attenuation of gastric cancer chemotherapy. *Adv. Healthc. Mater.* **2019**, *8*, 1900157. [[CrossRef](#)]
123. Garcia-Peiro, J.I.; Bonet-Aleta, J.; Bueno-Alejo, C.J.; Hueso, J.L. Recent advances in the design and photocatalytic enhanced performance of gold plasmonic nanostructures decorated with non-titania based semiconductor hetero-nanoarchitectures. *Catalysts* **2020**, *10*, 1459. [[CrossRef](#)]
124. Clavero, C. Plasmon-induced hot-electron generation at nanoparticle/metal-oxide interfaces for photovoltaic and photocatalytic devices. *Nat. Photonics* **2014**, *8*, 95–103. [[CrossRef](#)]
125. Ortega-Liebana, M.C.; Bonet-Aleta, J.; Hueso, J.L.; Santamaria, J. Gold-based nanoparticles on amino-functionalized mesoporous silica supports as nanozymes for glucose oxidation. *Catalysts* **2020**, *10*, 333. [[CrossRef](#)]
126. Luo, W.; Zhu, C.; Su, S.; Li, D.; He, Y.; Huang, Q.; Fan, C. Self-catalyzed, self-limiting growth of glucose oxidase-mimicking gold nanoparticles. *ACS Nano* **2010**, *4*, 7451–7458. [[CrossRef](#)]
127. Huo, M.; Wang, L.; Chen, Y.; Shi, J. Tumor-selective catalytic nanomedicine by nanocatalyst delivery. *Nat. Commun.* **2017**, *8*, 357. [[CrossRef](#)]